UNIVERSITY OF CALIFORNIA,
IRVINE

Polar Quantizer for Wireless Receivers: Theory, Analysis, and CMOS Implementation

THESIS

submitted in partial satisfaction of the requirements
for the degree of

MASTER OF SCIENCE

in Electrical Engeneering

by

Peyman Nazari

Thesis Committee:
Professor Payam Heydari Irvine, Chair
Associate Professor Ahmed Eltawil
Professor Ender Ayanoglu

2015

DEDICATION

To

my parents and friends

in recognition of their worth

Table of Contents

iii

List of Figures

List of Tables

ACKNOWLEDGMENTS

ABSTRACT OF THE THESIS

Polar Quantizer for Wireless Receivers: Theory, Analysis, and CMOS Implementation

By

Peyman Nazari

Master of Science in Electrical Engineering

University of California, Irvine, 2015

Professor, Payam Heydari, Chair

This thesis presents the theory and analysis of IF polar receiver (PRX) architecture. By using new quantization techniques in the polar domain, the proposed receiver can boost the signal to quantization noise ratio (SQNR) compared to a traditional rectangular (I/Q) receiver. The proposed PRX is composed of a magnitude and a phase quantizer. The magnitude quantizer is similar to the conventional rectangular quantizer in voltage domain. The phase quantizer employs a time-to-digital converter (TDC) for phase detection. Furthermore, an intuitive graphical method is used to analyze the quantization properties of the polar quantization. A 10 bit polar quantizer is designed and fabricated in 130nm CMOS, and achieves 2- to 5-dB of SQNR improvement compared to rectangular quantizer for signal bandwidths as high as 20MHz.

Introduction

Wireless receivers commonly process the received signal in the rectangular or I/Q domain. While polar architectures have been widely examined and used [2]-[5] in RF transmitters, signal processing and quantization in the polar domain in the RF receivers remains unexplored, with scattered theoretical analyses of polar quantizers studied in [6]-[9]. In [10] a CMOS GFSK transceiver was demonstrated, in which the phase information of the received signal is extracted in order to reconstruct the baseband data. In this thesis, we conduct a comprehensive analysis of polar detection and quantization; and introduce new techniques that can enhance the SQNR compared to rectangular quantization and relax the requirements on dynamic range and resolution of quantizers, under the same number of total quantization levels. Theoretical foundations are laid, numerical analysis is carried out, and implementation issues are studied and demonstrated. Finally, we demonstrate the design and implementation of a CMOS polar quantizer for cellular applications that achieves higher SQNR compared to rectangular quantizers

Implications on ADC design mean that such polar techniques can reduce power consumption, both from theoretical and implementation perspectives by saving one ADC, while achieving minimal degradation in SQNR. Likewise, we could achieve higher accuracy for approximately the same amount of consumed power as the rectangular technique. Also, the stringent requirement on dynamic gain control mechanism, as existed in a rectangular quantizer, will be relaxed.

As will be further revealed in this work, the proposed polar receiver (PRX) takes best advantage of the "bell-shaped" signal probability density functions (PDF), i.e., Gaussian or Rayleigh PDFs, found in most real life applications [11], [12]. The PRX finds a wide range of uses for wireless communication systems, because almost all modulation techniques involve complex signals. This

is especially true for an OFDM signal in which the signal distribution in complex plane is close to Gaussian PDF. Under realistic fading scenarios where the channel gain is usually modeled as a complex Gaussian (Rayleigh) or Rician random variable, and as we will see later, a PRX demonstrates great advantage in the SQNR improvement over a rectangular receiver. Furthermore, certain wireless signals have a high peak-to-average power ratio (PAPR), and this property can be exploited as an advantage in the PRX. Another application of the PRX is in the ultrasound systems [13], [14], where the signal of interest is complex. In these systems, Doppler information for blood flow velocity and frequency is conveyed in the phase of the received signal, while the depth information is conveyed in the magnitude signal.

In addition, with the advancement of digital CMOS, the maximum achievable magnitude resolution is decreased with continuous scaling of low supply voltage and device feature size, whereas the phase resolution (in time-to-digital converters) is increased by the faster transition times and higher f_{max} of nano-scale CMOS. Hence, in contrast to magnitude detection, the phase detection in time domain is amenable to technology scaling. As a result, since part of the quantization process takes place in the phase domain, the proposed PRX exploits such advantages. Also, since the dynamic range of the phase signal is independent of the signal power, polar quantization relaxes the required dynamic range of the quantizer for the phase path, thereby relaxing the gain control mechanism of the receiver.

Receiver Architecture

Modern wireless communication systems need to accommodate sending/transmitting of wideband signals with sophisticated modulation schemes (e.g., 20MHz, 64QAM OFDM for LTE [15], and thereby achieving high data-rate. It not only translates to more challenging RF performance requirements in terms of linearity, noise figure (NF) and dynamic range, but also sets forth stringent requirements on the analog to digital converter (ADC) in terms of its resolution and speed. A high resolution high speed ADC that satisfies all these requirements would be power hungry, directly contributing to higher power dissipation of the RX and shorter battery life.

We should also emphasize that, in the world of modern digital communication, wireless signals contain information in both their instantaneous magnitude and phase components to maximally utilize the available bandwidth, thereby maximizing the spectral efficiency.

$$s(t) = A(t)\cos(\omega_{Rf}t + \phi(t)) \tag{1}$$

This demands the baseband equivalent signal, S_{BB}(t), to be a complex signal in nature. The real and imaginary part of such signal is usually denoted as in-phase (I) and quadrature (Q) components.

$$s_{BB}(t) = A(t)e^{j\phi(t)} = I_{BB}(t) + jQ_{BB}(t) \tag{2}$$

$$I_{BB}(t) = A(t).\cos(\phi(t)), Q_{BB}(t) = A(t).\sin(\phi(t)) \tag{3}$$

The receiver job is to detect and the RF signal and extract the base-band information to reconstruct S_{BB}(t). A rectangular IQ receiver block diagram is shown in Figure 1. Quadrature LO and mixer and I/Q receive path are used to detect the real and imaginary part of the baseband complex signal.
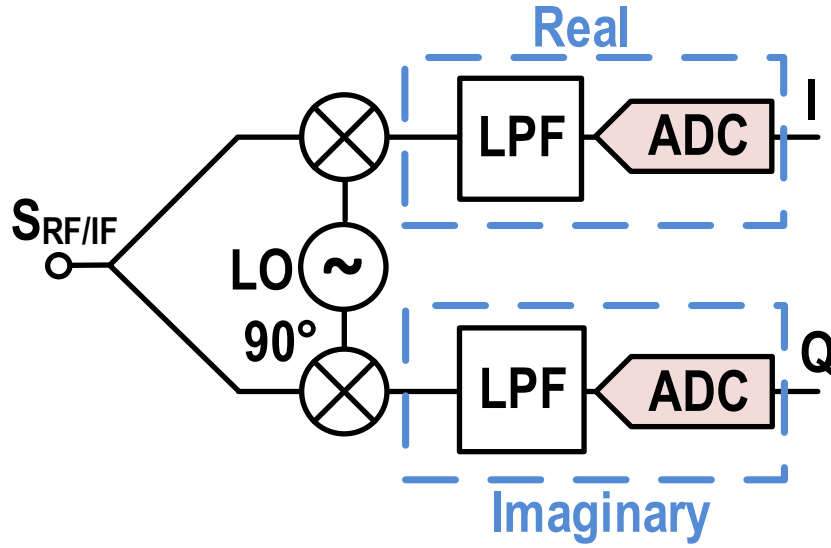
Figure 1 Rectangular (I/Q) receiver architecture

The quantized signal at the output of each I/Q ADC contains a certain amount of noise added to the either I or Q component of the signal. While channel and RF-front end noise appear in the total output noise, quantization noise of ADCs also contribute to the total noise. Thereby, the detected signal is only an estimation of the original signal:

$$\hat{s}_{BB}(t) = \hat{A}(t)e^{j\hat{\phi}(t)} = \hat{I}_{BB}(t) + j\hat{Q}_{BB}(t) \tag{4}$$

$$s_{BB}(t) = \hat{s}_{BB}(t) + n(t) \tag{5}$$

The receiver in cellular radios typically deals with non-line-of-sight (NLOS) condition. Thus when the receiver is not mobile relative to the transmitter, the channel is considered to be a flat fading channel (FFC) and the received signal is characterized with a complex Gaussian probability distribution function (PDF). This attribute can be exploited to design quantizers with high SQNRs. The distribution of the Gaussian signal in complex plane is concentrated around the origin compared to that of a uniform signal (Figure 2). The magnitude of a Gaussian signal has a Rayleigh PDF, implying that high amplitudes are less likely to occur. While a conventional I/Q receiver tries

4

to detect the real and imaginary parts of the received signal (Figure 2 (b)), as was shown in [3], the uniform rectangular quantization does not produce minimum quantization noise, since it allocates equal quantization steps over the input dynamic range regardless of the magnitude of the input signal and its probability of occurrence. An alternative approach is to detect its phase and magnitude, i.e. A and ϕ, and quantize them to reconstruct the signal in digital domain. While in each phase and magnitude domain, the quantization takes place uniformly, the area of quantization segments become smaller, as the signal magnitude becomes smaller, leading to a lower quantization error. Since the probability of receiving signals with high amplitudes is much lower than that of signals with average amplitudes, the average quantization error will be lower in this type of quantization, as will be seen in Chapter 2.

(a)   (b)
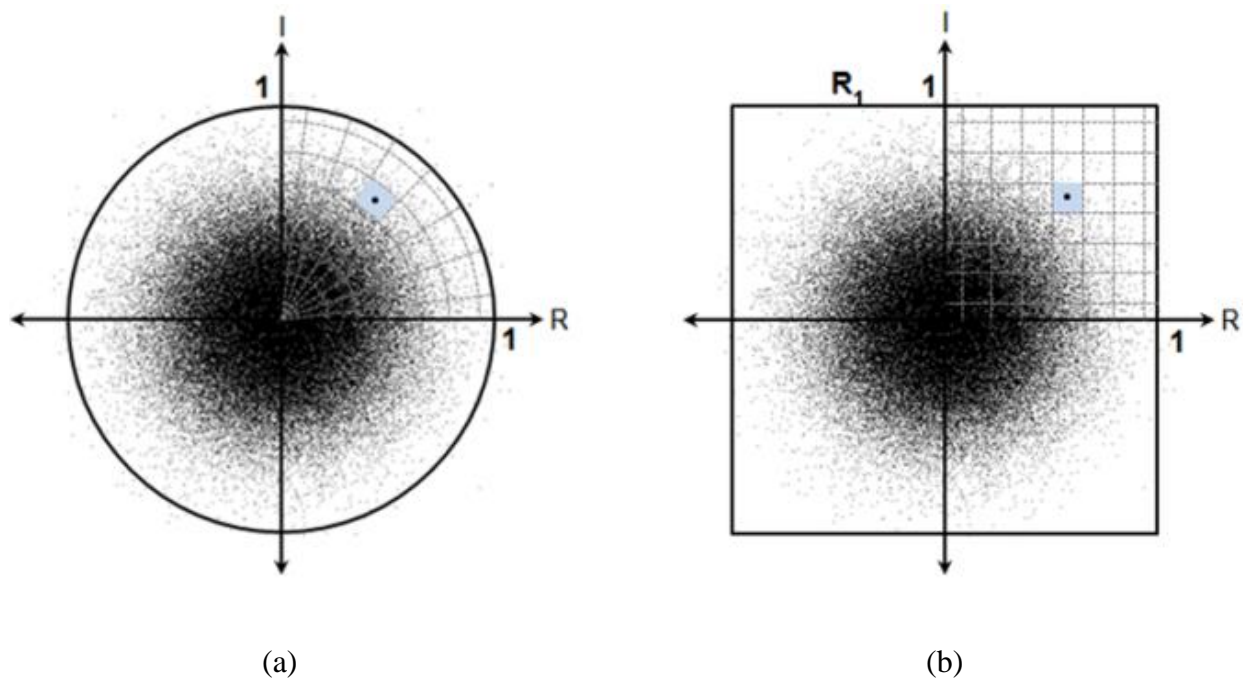
Figure 2 Distribution of a Gaussian signal in complex plane. (a) Polar quantization; (b) Rectangular quantization

One can imagine to design a receiver that detects RF signal and extracts the magnitude and phase information from the modulated RF signal. The quantized outputs are the quantized magnitude

and phase, $\hat{A}$ and $\hat{\phi}$, respectively. The complex baseband signal, $\hat{S}_{BB}$(t), is then reconstructed in the digital domain.

$$\hat{s}_{BB}(t) = \hat{A}(t)e^{j\hat{\phi}(t)} = \hat{I}_{BB}(t) + j\hat{Q}_{BB}(t) \tag{6}$$

One potential candidate to implement a complex detector/quantizer that processes the baseband signal in the magnitude/phase domain, i.e. a "Polar Receiver", is shown in Figure 3. An envelope
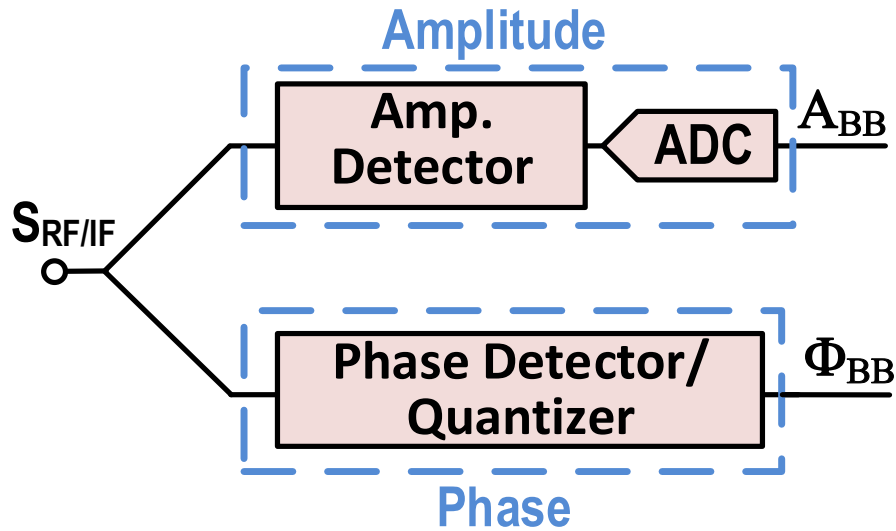
Figure 3 A hypothetical polar receiver architecture

detector followed by an analog-to-digital voltage convertor is responsible for magnitude quantization. The quantization takes place in the voltage domain. The phase detector needs to extract the timing information of the RF/IF signal, $S_{RF/IF}$. This can be done by comparing the zero crossings of the signal against a known reference. The details of the circuit implementation are discussed in Chapter 4.

Complex Signal Quantization

1.1 Graphical Representation

Rectangular and polar quantizers are viewed graphically in the complex plane of **Error! Reference source not found.**. The rectangular quantizer (bold dashed line) and the polar quantizer (bold solid line) cover different input PDFs. The maximum magnitude level of these quantizers is determined by the full scale of the quantizer. For the rest of the section, the quantization levels are assumed to be uniformly distributed in the I/Q domain for the rectangular quantizer, and also in the magnitude/phase domain for the polar quantizer.

The samples of the input signal to be quantized are represented by the small black-dots as shown in **Error! Reference source not found.**. The distribution of the input signal depends on its PDF, while its average magnitude depends on how the signal is scaled (i.e., with a variable gain amplifier (VGA)) before the quantizer. Indeed, the maximum magnitude of the input signal should be scaled depending on how many (if any) overload samples – defined as samples where the signal exceeds the full scale of the quantizer – can be tolerated. A key point to be demonstrated later is how well these black-dots "fit" into the quantizers. Those cases where the black-dots input signals take up most of the quantization region with little wasted space imply high quantization efficiency, as will be mathematically shown later in this Chapter.

Now consider the case in Figure 4, where the black dots represents samples of the complex input signal with uniform rectangular distribution and the rectangular quantization covers the R1 rectangular region outlined by the bold dashed line. With this input signal, the polar quantization should use the C1 circular region outlined by the bold solid line in order to avoid overloading samples. Because the area of the C1 circle in Figure 4 is larger than that of the R1 rectangle, the
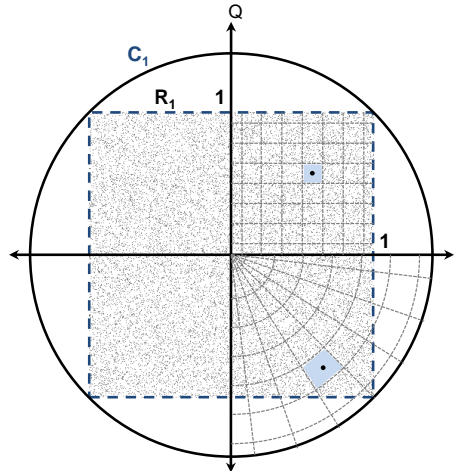
Figure 4 The rectangular shaped uniform input distribution (black dots) with the polar and rectangular quantization. The total quantization levels are fixed.

SQNR of rectangular quantization would then be higher than that of the polar quantization of the C1 circle.

Figure 5**Error! Reference source not found.** represents the scenario in which the input has circular uniform distribution. The black dots of input signal represent samples of the complex input signal with complex uniform circular distribution, and the polar quantizer covers the C2 circular region outlined by the bold solid line (Figure 5). To avoid overloading samples, the rectangular
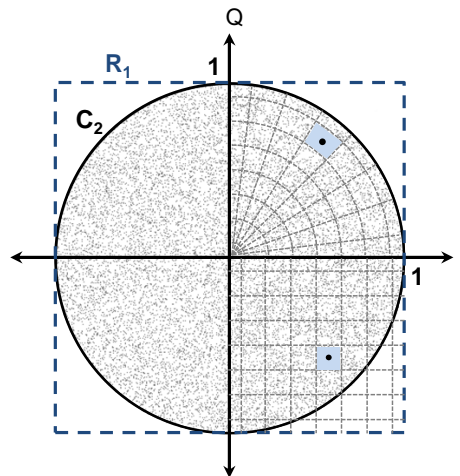
Figure 5 The circular shaped uniform input distribution with the polar and rectangular quantization

quantizer should use the R1 rectangular space, but it is not well fit for the circular input distribution in **Error! Reference source not found.**. Hence, the C2 polar quantizer with the circular uniform input distribution has better quantization efficiency, and therefore, smaller quantization error compared to the R1 rectangular quantizer.

Shown in Figure 6 are samples of a signal with complex Gaussian distribution, which is approximately of a circular shape. Therefore, polar quantizer with its intrinsically circular coverage better approximates the signal than a rectangular quantizer. Also, the input signal samples mostly fall in quantization cells in the vicinity of origin due to the nature of Gaussian PDF. This attribute results in higher SQNR for polar quantizer compared to that of rectangular quantizer, because quantization cells close to origin are smaller in size than the ones in a rectangular quantizer.
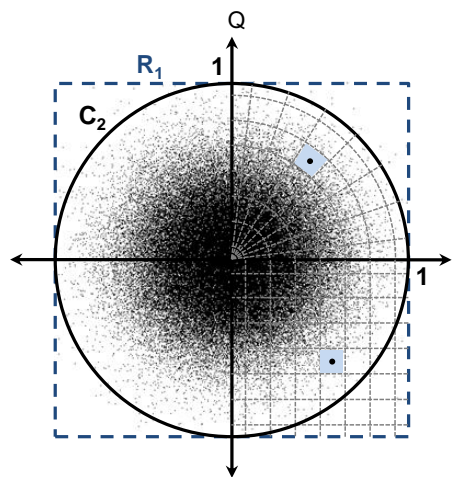
Figure 6 The complex Gaussian input distribution with the polar and rectangular quantization
The total quantization levels are fixed.

In addition, for the same full-scale range, the magnitude part in a polar quantizer needs smaller dynamic range compared to that of I and Q in rectangular quantizer, simply because the magnitude -as we define in this work- always takes positive values (the polarity of the magnitude can be

absorbed into the phase without sacrificing the generality of polar representation of a complex signal [1]). The dynamic range of the phase component is independent of the input signal level, another advantage of polar quantizer, which will be explored in great details in Section 2.3.

1.2 Quantization Error Properties

This section analyzes the quantization errors for both the rectangular and polar quantizers. We calculate the maximum quantization error of rectangular quantizer for arbitrary numbers of I / Q bits (B_i / B_q) and that of polar quantizer for arbitrary numbers of magnitude/phase bits (B_m / B_p)
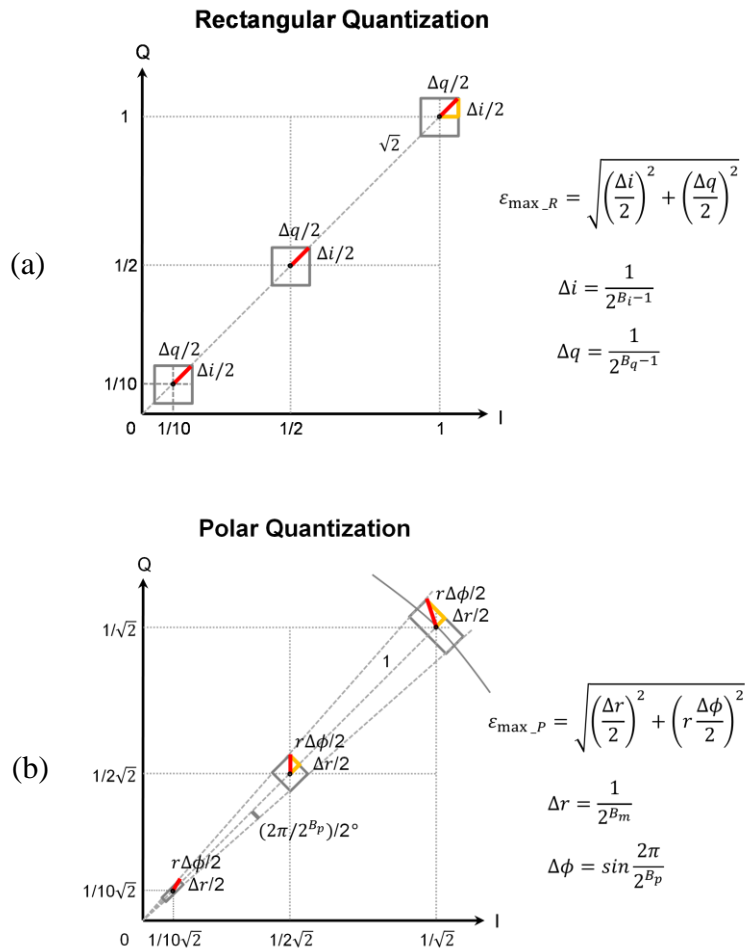
Figure 7 The complex B_i / B_q rectangular and B_m / B_p polar quantization errors with a different input level. (a) The maximum quantization level is $\sqrt{2}$ (=R_1 rectangle), (b) the maximum quantization level is 1 (=C_2 circle)

(Figure 7). The magnitude of the rectangular quantization consists of 2^{Bi} and 2^{Bq} levels, covering a normalized range from -1 to 1 for both I and Q. For the polar quantizer, the magnitude quantizer consists of 2^{Bm} levels covering normalized range from 0 to 1. The phase quantization has 2^{Bp} levels covering 0 to 2π.

For rectangular quantizer, the shape of each quantization cell on the complex plane is a rectangle with width and height of Δi and Δq as seen in Figure 7(a). Δi and Δq are the lengths of one in-phase and one quadrature-phase quantization intervals, respectively and are expressed as

$$\Delta i = \frac{1}{2^{B_i-1}} , \Delta q = \frac{1}{2^{B_q-1}} \tag{7}$$

The complex value of the center point of a quantization cell is assigned as the quantized level to all quantizer inputs falling within that cell. The quantization error (ε_R) is the distant between the input and the center of the cell. It is evident that the maximum quantization error occurs when the input is on one of the four corners of a cell where it has the maximum distant from the center of the cell. The maximum quantization error of B_i / B_q rectangular quantizer ($\varepsilon_{max,R}$) is then calculated to be

$$\varepsilon_{max,R} = \sqrt{\left(\frac{\Delta i}{2}\right)^2 + \left(\frac{\Delta q}{2}\right)^2} = \sqrt{\left(\frac{1}{2} \cdot \frac{1}{2^{B_i-1}}\right)^2 + \left(\frac{1}{2} \cdot \frac{1}{2^{B_q-1}}\right)^2}$$

$$= \sqrt{\frac{1}{2^{2B_i}} + \frac{1}{2^{2B_q}}} \tag{8}$$

We can find the relationship between B_i and B_q if we assume total number of quantization cells to be a constant $M=2^N$. Under this assumption we have

11

$$2^{B_i} \times 2^{B_q} = M \quad \Rightarrow B_i + B_q = N \tag{9}$$

We can find the optimum bit distribution between I and Q components to minimize $\varepsilon_{max,R}$, under this constraint by setting $\partial\varepsilon_{max,R}/\partial B_i = 0$

$$\frac{\partial\varepsilon_{max,R}}{\partial B_i} = \frac{1}{2\varepsilon_{max,R}} \times 2ln2\left(2^{-2(N-B_i)} - 2^{-2B_i}\right) = 0 \tag{10}$$

$$\Rightarrow B_i = B_q = N/2 = B_r$$

It is seen from (10) that $\varepsilon_{max,R}$ is minimized when bits are divided equally between I and Q, thus each quantization cell is a square with the length of $\Delta i = \Delta q = 1/(2^{N/2-1})$.

In this case, (8) can be simplified to

$$\varepsilon_{max,R} = \sqrt{\frac{1}{2^{2B_r-1}}} = \sqrt{\frac{1}{2^{N-1}}} \tag{11}$$

Similarly, for polar quantizer, the shape of each quantization cell on the complex plane is a segment with radial length and angular width of Δr and $\Delta\phi$ as seen in Figure 7(b). Δr and $\Delta\phi$ are the lengths of one magnitude and one phase quantization intervals, respectively and are expressed as

$$\Delta r = \frac{1}{2^{B_r}} \quad , \Delta\phi = \frac{2\pi}{2^{B_p}} \tag{12}$$

The complex value of the center point of a quantization cell is assigned as the quantized level to all quantizer inputs falling within that cell. The quantization error (ε_P) is the distant between the input and the center of the cell. It is evident that the maximum quantization error occurs when the input is on one of the two outermost corners of a cell where it has the maximum distant from the

center of the cell. The maximum quantization error of B_m / B_p polar quantizer ($\varepsilon_{max,P}$) is then calculated to be

$$\varepsilon_{\mathrm{max},P} = \sqrt{\left(\frac{\Delta r}{2}\right)^2 + \left(r\frac{\Delta\phi}{2}\right)^2} = \sqrt{\left(\frac{1}{2}\cdot\frac{1}{2^{B_m}}\right)^2 + \left(\frac{r}{2}\cdot\frac{2\pi}{2^{B_p}}\right)^2} \qquad (13)$$

where Δr and $r\Delta\phi$ are the lengths of one magnitude and one phase quantization intervals, respectively. r is the normalized magnitude quantization level ($1/2^{B_m} \leq r \leq 1$).

In (13), it is assumed that B_p is large such that the angular width $\Delta\phi$ is small enough to have

$$\Delta\phi \cong sin\Delta\phi \qquad (14)$$

It is evident from (13) that $\varepsilon_{max,P}$ depends on the magnitude of the input signal r. It is noteworthy that $\varepsilon_{max,P}$ increases as r increases.

It is important to understand how maximum quantization error (ε_{max}) relates to the input signal level. The maximum quantization errors of rectangular and polar quantization are shown in Fig. 2. It is clearly seen that for rectangular quantization, ε_{max} is independent of input level, since the quantization cells are equally sized. On the other hand, a unique property of the polar quantization is that it has the lowest ε_{max} at the lowest input level and the highest ε_{max} at the highest input level. This is because the cells close to the origin are smaller in area compared to the ones close to the boundary of the quantizer (edge of the circle). As will be seen in next section, these qualities of the polar quantization will be exploited favorably to improve the SQNR compared to the rectangular quantization for complex Gaussian signals.

By equating (11) to (13) the maximum input magnitude for which the quantization error of a polar quantizer remains smaller than that of a rectangular quantizer is obtained;

$$\sqrt{2\left(\frac{1}{2^{B_r}}\right)^2} = \sqrt{\left(\frac{1}{2^{B_m+1}}\right)^2 + \left(\frac{r_{max}}{2} \cdot \left(\frac{2\pi}{2^{B_p}}\right)\right)^2}$$

$$r_{max} \approx \frac{2^{B_p}}{2\pi}\sqrt{\frac{8}{2^{2B_r}} - \frac{1}{2^{2B_m}}} \tag{15}$$

Moreover, If we assume that the magnitude quantizer uses the same ADC as the I and Q quantizers (i.e. $B_m=B_r$), then (3) is simplified to:

$$r_{max} = \frac{\sqrt{7} \cdot 2^{B_p}}{2\pi \cdot 2^{B_m}} \tag{16}$$

In Figure 8, the maximum errors of polar and rectangular quantizers are shown as a function of input signal magnitude. Unlike the rectangular quantizer, the minimum and maximum values of polar quantization error depend on the magnitude and phase resolution which means when the input magnitude is increased, $\varepsilon_{max,R}$ is fixed and $\varepsilon_{max,P}$ is increased. This graph indicates that ε_{max} of the low magnitude input signals is dominated by the magnitude resolution and ε_{max} of large
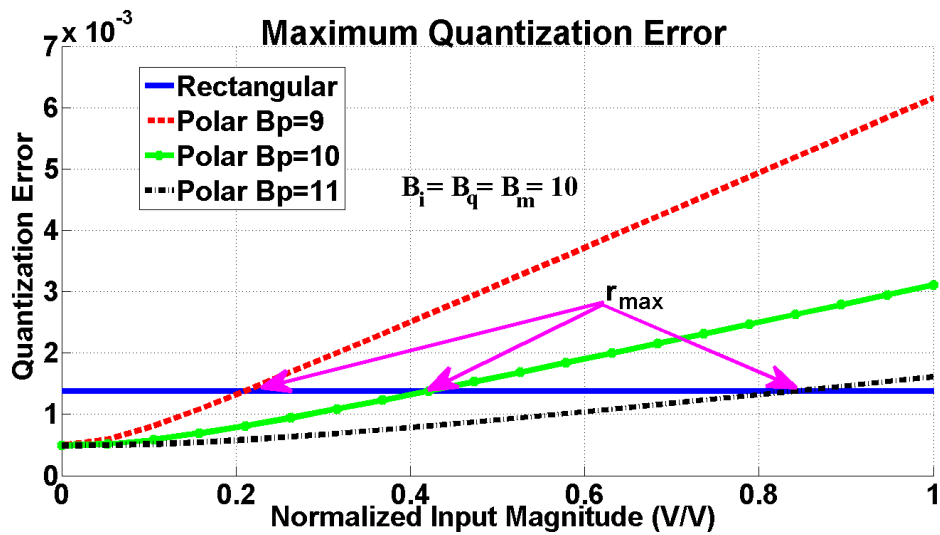
Figure 8 The maximum quantization error for rectangular and polar quantizer

magnitude input signals is dominated by the phase resolution. Basically for $B_m=B_p$, r_{max} equals to 0.42. According to different allocation of B_m/B_p polar quantizer, the cross point between polar and rectangular is changed. If average value of a complex Gaussian PDF is less than r_{max} then the SQNR is expected to be higher for polar quantizer compared to rectangular quantizer.

As evident from (13) and also seen from Figure 8, the minimum error for poplar quantizer occurs at the smallest input level. This minimum error, $\min\{\varepsilon_{\max,P}\}$, only depends on the magnitude resolution:

$$\min\{\varepsilon_{\max,P}\} = \frac{1}{2} \cdot \frac{1}{2^{B_m}} \tag{17}$$

From (11) and (17) the ratio between $\min\{\varepsilon_{\max,P}\}$, and $\varepsilon_{\max,R}$ can be calculated:

$$\frac{\min\{\varepsilon_{\max,P}\}}{\varepsilon_{\max,R}} = \frac{1}{2\sqrt{2}} \cdot \frac{2^{B_r}}{2^{B_m}} \tag{18}$$

As can be seen from (18), under same resolution for magnitude and I/Q ($B_m = B_r$), polar quantization can reduce the maximum quantization error roughly by a factor of $2\sqrt{2}$ for low power signals. On the other hand, the maximum error, $\max\{\varepsilon_{\max,P}\}$, is heavily dependent on the phase resolution. The ratio between the minimum and maximum error is determined by the ratio between number of magnitude and phase quantization intervals, i.e. the difference between B_m and B_p:

$$\frac{\max\{\varepsilon_{\max,P}\}}{\min\{\varepsilon_{\max,P}\}} = \sqrt{1 + 4\pi^2 \frac{2^{2B_m}}{2^{2B_p}}} \tag{19}$$

Under the the assumption of constant total number of bits ($B_m+B_p = const.$), the choice of optimum resolution allocation and distribution of bits between magnitude and phase depends on the statistical characteristics of the signal such as the average magnitude and the occurrence likelihood of signals with very low or very high magnitude. As an example a complex signal with a complex

Gaussian distribution is considered. The magnitude of such signal follows a Rayleigh distribution which is shown in Figure 9 (a). The expected value (average) of the maximum quantization error can be calculated by multiplying $\varepsilon_{max,P}(r)$ by the probability distribution function of the Rayleigh distribution, $P_R(r)$:

$$E[\varepsilon_{max}] = \iint P_{R,\theta}(r,\theta) . \varepsilon_{max}(r,\theta). drd\theta = \int P_R(r). \varepsilon_{max}(r). dr \qquad (20)$$

The integrand in the one dimensional integral in (20) is plotted for several values of B_m and B_p of polar quantizer and for a 10 bit rectangular quantizer in Figure 9. The area underneath each curve determines the expected maximum quantization error (average of $\varepsilon_{max,P}$). A rough comparison between the performances of these quantizer can be made by qualitative inspection of the area under these curves. A quantitative analysis and comparison is provided in the next Chapter.
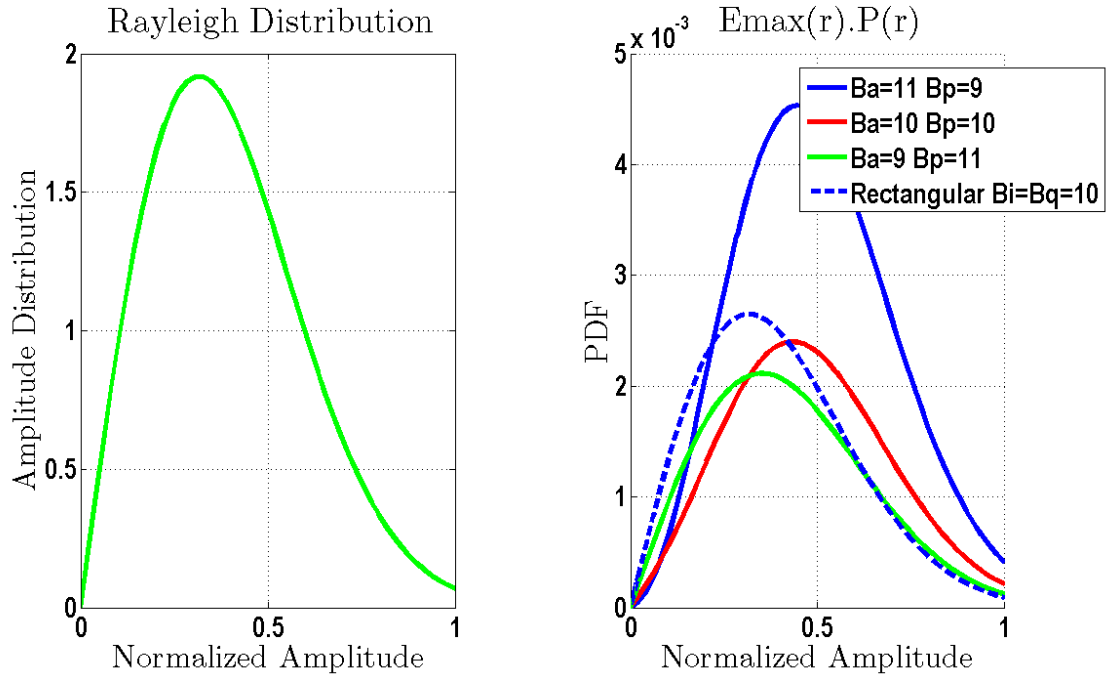
Figure 9 (a) Rayleigh distribution, (b) integrand in the one dimensional integral in (20)

1.3 The Effect of Input Signal PDFs on Rectangular and Polar Quantization Errors

To compare polar and rectangular quantizers under different distributions of the input signal, we study SQNR as a function of average input magnitude.

1.3.1 Complex Uniform Rectangular Distribution

1.3.1.1 RECTANGULAR QUANTIZER

First, we assume uniform rectangular distribution for the input signal, with its I and Q components varying from $-a_r$ to a_r. The mean square quantization error (MSE) of the signal lying in each cell Q_k with an area of A_k ($\overline{\varepsilon_{rr,k}^2}$) (see Figure 10) is expressed as:
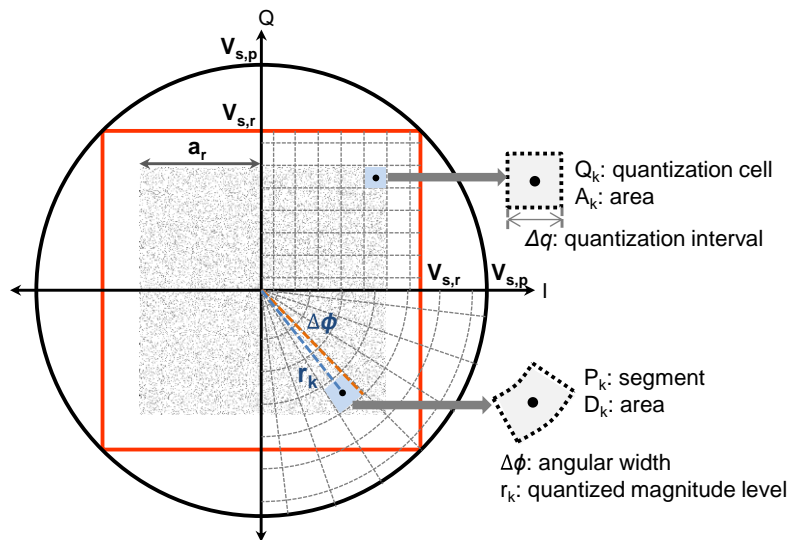
Figure 10 Denotation of rectangular and polar quantizers for uniform rectangular input distribution

$$\overline{\varepsilon_{rr,k}^2} = E[\varepsilon^2 | s \in Q_k] = \int\limits_{r_k - \Delta q/2}^{r_k + \Delta q/2} \int\limits_{r_k - \Delta q/2}^{r_k + \Delta q/2} ((x - r_k)^2 + (y - r_k)^2) \frac{dxdy}{A_k} = \frac{\Delta q^4}{6A_k}$$

$$= \frac{\Delta q^2}{6}$$

(21)

where $\Delta q = 2V_{s,r}/2^{Br}$ denotes the length of a quantization interval, and s is the received signal (Figure 10). The average quantization error $\overline{\varepsilon_{rr}^2}$ is then calculated to be:

$$\overline{\varepsilon_{rr}^2} = \sum_{k=1}^{M} \overline{\varepsilon_{rr,k}^2} \cdot \frac{A_k}{R} = \frac{M\Delta q^4}{6 \times 4V_{s,r}^2} \cong \left(\frac{2a_r}{\Delta q}\right)^2 \frac{\Delta q^2}{6} \cdot \frac{\Delta q^2}{4a_r^2} = \frac{\Delta q^2}{6}$$

(22)

where probability of lying s on Q_k is determined by A_k/R and R is the area of the rectangle where the uniformly distributed signal lies in it. Σ_k denotes the summation over quantization cells which the input signal may fall into. M is the total number of cells lying within the distribution region of the input signal. It is evident that $\overline{\varepsilon_{rr}^2}$ is independent of the signal power.

(22) can be expressed in terms of number of bits for I and Q components B_r and full scale magnitude of the rectangular quantizer $2V_{s,r}$:

$$\overline{\varepsilon_{rr}^2} = \frac{2}{3} \frac{V_{s,r}^2}{2^{2B_r}}$$

(23)

1.3.1.2 SIGNAL POWER AND SQNR

The signal to quantization noise ratio (SQNR) can be calculated by dividing the average signal power (μ_r^2) to the average quantization noise power, $\overline{\varepsilon_{rr}^2}$. The average power of a signal with uniform rectangular distribution (μ_r^2) is calculated as:

$$\mu_r^2 = \int\limits_{-a_r}^{a_r} \int\limits_{-a_r}^{a_r} (x^2 + y^2)\frac{dxdy}{R} = \frac{2a_r^2}{3} \tag{24}$$

From (24), SQNR of a rectangular quantizer for a signal with uniform rectangular distribution, ρ_{rr} is obtained:

$$\rho_{rr} = \frac{3}{2}\frac{\mu_r^2}{V_{s,r}^2}\, 2^{2B_r} = \frac{a_r^2}{V_{s,r}^2}\, 2^{2B_r} \tag{25}$$

It is evident from (25) that SQNR linearly increase with signal power in this case (see Figure 5).

1.3.1.3 POLAR QUANTIZER

The MSE of the signal lying in cell P_k with an area of D_k (Figure 10) in polar quantizer $(\overline{\varepsilon_{rp,k}^2})$ is:

$$\overline{\varepsilon_{rp,k}^2} = E[\varepsilon^2|s \in P_k]$$

$$= \frac{1}{D_k} \int_{-\frac{\Delta\phi}{2}}^{\frac{\Delta\phi}{2}} \int_{-\frac{\Delta r}{2}}^{\frac{\Delta r}{2}} \{r_k{}^2 + (r_k + \delta r)^2 - 2r_k(r_k + \delta r)\cos\theta\}\, d(\delta r)(r_k$$

$$+ \delta r)d\theta$$

$$= \frac{r_k\Delta r}{12D_k}\cdot\left(3\Delta\phi(8r_k^2 + \Delta r^2) - 4(12r_k^2 + \Delta r^2)\sin\frac{\Delta\phi}{2}\right) \tag{26}$$

where r_k is the distance of the center of P_k from origin and $\Delta\phi$ is its angular width (Figure 10).

$sin\frac{\Delta\phi}{2}$ can replaced by its third order Taylor expansion assuming a small $\Delta\phi$, i.e. sufficiently high phase resolution.

$$\sin\left(\frac{\Delta\phi}{2}\right) \cong \frac{\Delta\phi}{2} - \frac{\left(\frac{\Delta\phi}{2}\right)^3}{3!} \tag{27}$$

Using this expansion of $sin \frac{\Delta \phi}{2}$, (26) is simplified to:

$$\overline{\varepsilon_{rp,k}^2} = \frac{1}{12D_k} \left(r_k \Delta r^3 \Delta \phi + r_k^3 \Delta r \Delta \phi^3 \right) \tag{28}$$

The MSE of polar quantizer for a signal with uniform rectangular distribution, $\overline{\varepsilon_{rp}^2}$, is expressed in a similar way as for rectangular quantizer:

$$\overline{\varepsilon_{rp}^2} = \sum_k \overline{\varepsilon_{rp,k}^2} \cdot \frac{D_k}{R} = \frac{1}{R} \left(\Delta r^3 \Delta \phi \sum_k r_k + \Delta \phi^3 \Delta r \sum_k r_k^3 \right) \tag{29}$$

Assuming high magnitude and phase resolutions, we can replace Σr_k and Σr_k^3 in (9) and (10) with integration, i.e.,

$$\sum_k r_k \approx \frac{1}{\Delta r} \sum_{p=1}^{p=2^{B_p}} \int_0^{\frac{a_r}{\cos \theta_p}} r. \, dr = \frac{1}{\Delta r} \sum_{p=1}^{p=2^{B_p}} \frac{a_r^2}{2 \cos^2 \theta_p}$$

$$\approx \frac{a_r^2}{2 \Delta r \Delta \phi} \cdot 8 \cdot \int_0^{\frac{\pi}{4}} \sec^2 \theta \cdot d\theta = \frac{4 a_r^2}{\Delta r \Delta \phi} \tag{30}$$

and

$$\sum_k r_k^3 \approx \frac{1}{\Delta r} \sum_{p=1}^{p=2^{B_p}} \frac{a_r^4}{4 \cos^4 \theta_p} \approx \frac{a_r^4}{4 \Delta r \Delta \phi} \cdot 8 \times \int_0^{\frac{\pi}{4}} \sec^4 \theta \cdot d\theta == \frac{8 a_r^4}{3 \Delta r \Delta \phi} \tag{31}$$

Thus, using (30) and (31), (29) is expressed as:

$$\overline{\varepsilon_{rp}^2} = \frac{\Delta r^2}{12} + \frac{a_r^2 \Delta \phi^2}{18} \tag{32}$$

(32) is expressed in terms of polar quantizer full scale $V_{s,p}$ and number of bits for magnitude and phase parts, B_m, B_p, respectively:

$$\overline{\varepsilon_{rp}^2} = \frac{1}{12} \cdot \frac{V_{s,p}^2}{2^{2B_m}} + \frac{2\pi^2}{9} \frac{a_r^2}{2^{2B_p}} = \frac{1}{12} \cdot \frac{V_{s,p}^2}{2^{2B_m}} + \frac{\pi^2}{3} \frac{\mu_r^2}{2^{2B_p}} = \tag{33}$$

It is seen from (33) that $\overline{\varepsilon_{rp}^2}$ has a term linearly increasing with signal power added to a constant term. From (33) and (24), SQNR of a polar quantizer for a signal with uniform rectangular distribution, ρ_{rp} is obtained:

$$\rho_{rp} = \frac{\mu_r^2}{\frac{1}{12} \cdot \frac{V_{s,p}^2}{2^{2B_m}} + \frac{2\pi^2}{9} \frac{a_r^2}{2^{2B_p}}} = \frac{\mu_r^2}{\frac{1}{12} \cdot \frac{V_{s,p}^2}{2^{2B_m}} + \frac{\pi^2}{3} \frac{\mu_r^2}{2^{2B_p}}} \tag{34}$$

For the polar and rectangular quantizers under uniform rectangular input distribution shown in Figure 10, $V_{s,p}$ should be $\sqrt{2}$ times higher than $V_{s,r}$, so that the polar quantizer fully covers input signal distribution. It is clearly seen from (33) that the error power grows with input signal power (μ_r^2), resulting in saturated SQNR as the input power increases. Moreover, according to (33), the slope of this increase can be reduced by increasing phase bits. To verify the analysis, the SQNR

Figure 11 The simulated SQNR comparison between the 7Bi/7Bq uniform rectangular quantizer (R7.0/7.0) and various uniform polar quantizers (different M/P allocation) for Btot fixed at 14 bits for Rectangular uniform input PDF

of both polar and rectangular quantizers were simulated under various combinations of B_m/B_p quantization levels in the polar quantizer, assuming that the total number of quantization levels is fixed at $B_{tot} = 14$ bits. Similarly, for rectangular quantizer $B_r = B_{tot}/2 = 7$. Figure 11 shows the simulation results, demonstrating saturating SQNR for polar quantizer. The calculated values of SQNR for both polar and rectangular quantizers, ρ_{rr} and ρ_{rp} are also plotted on the same figure to confirm the agreement between theory and simulation.

To compare the performance of rectangular and the polar quantizers for signals with uniform rectangular distribution, we calculate the ratio of the SQNR associated with rectangular quantizer over that of the rectangular quantizer, α_r, noting that $V_{s,p} = \sqrt{2}\, V_{s,r} = \sqrt{2}\, V_s$. For this comparison, we also assume $B_m + B_p = 2B_r$. Therefore we have:

$$\alpha_r = \frac{\rho_{rr}}{\rho_{rp}} = \frac{\frac{3}{2}\mu_r^2/V_s^2 \cdot 2^{2B_r}}{\frac{1}{12}\cdot\frac{2V_s^2}{2^{2(2B_r-B_p)}} + \frac{\pi^2}{3}\frac{\mu_r^2}{2^{2B_p}}} = \frac{2^{2(B_p-B_r)}}{4} + \frac{\pi^2}{2}\frac{\mu_r^2}{V_s^2}\, 2^{2(B_r-B_p)} \tag{35}$$

Figure 12 compares the SQNR of a polar quantizer against that of a rectangular quantizer for signals with uniform rectangular distribution, when the number of phase bits runs from 4 to 10 under the assumption of constant number of bits ($B_m + B_p = 2B_r = 14$ in this case).

It is clear from this figure that even under optimal magnitude/phase bit allocation for polar quantizer, the rectangular quantizer achieves a higher SQNR, when the input signal follows a
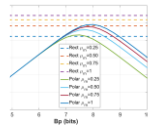
Figure 12 The SQNR comparison between the 7Bi/7Bq uniform rectangular and (14-Bp)/Bp polar quantizers for a signal with uniform rectangular distribution; μrn is the normalized signal power
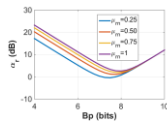
Figure 13 The SQNR ratio between the 7Bi/7Bq uniform rectangular and (14-Bp)/Bp polar quantizers for a signal with uniform rectangular distribution; μrn is the normalized signal power

uniform rectangular distribution. This result was indeed expected, since a uniform rectangular signal better fits in a rectangular quantizer with less wasted quantized area on the complex plane. To better illustrate this fact the SQNR ratio, α_r, is also plotted in Figure 13 which indicates that for a signal with uniform rectangular distribution, rectangular quantizer achieves higher SQNR compared to a polar quantizer for any signal power below the quantizer full-scale.

Figure 13 indicates that for signals with uniform rectangular distribution, polar quantizer achieves same SQNR as the rectangular quantizer ($\alpha_r = 0$dB), only for low signal powers. This is due to the dominancy of phase quantization for small signal magnitudes.

1.3.2 Complex Uniform Circular Distribution

Second, we assume that the input signal has a circular uniform distribution (Figure 14). We now calculate the MSE of this distribution under rectangular quantization.
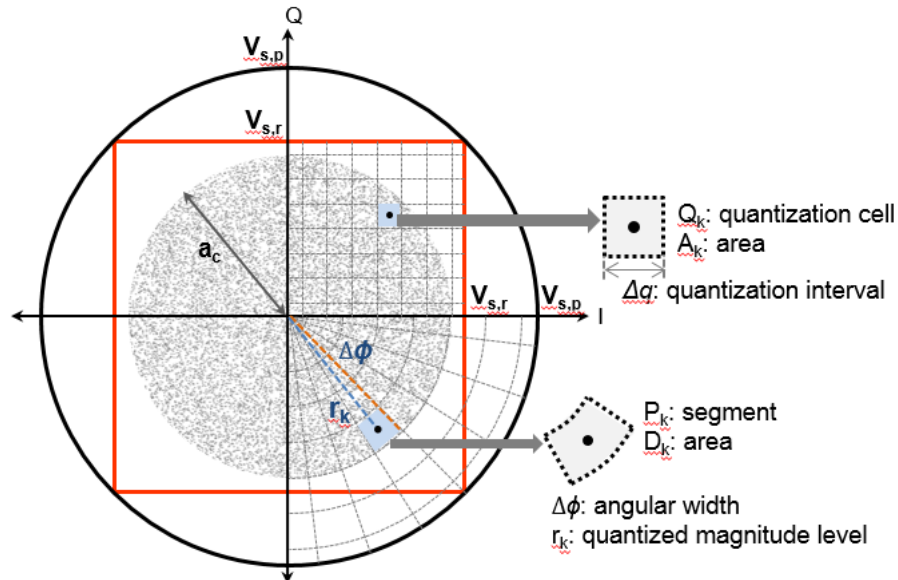
Figure 14 Denotation of rectangular and polar quantizers for uniform circular input distribution

1.3.2.1 RECTANGULAR QUANTIZER

The MSE in each section is identical to (21), which is presented here for the sake of completeness.

$$\overline{\varepsilon_{cr,k}^2} = E[\varepsilon^2|s \in Q_k] = \int\limits_{r_k-\Delta q/2}^{r_k+\Delta q/2} \int\limits_{r_k-\Delta q/2}^{r_k+\Delta q/2} ((x-r_k)^2 + (y-r_k)^2)\frac{dxdy}{A_k} = \frac{\Delta q^4}{6A_k}$$

$$= \frac{\Delta q^2}{6} \tag{36}$$

Therefore, the MSE is determined by the number of cells covering the input distribution:

$$\overline{\varepsilon_{cr}^2} = \sum_k E[\varepsilon^2|s \in Q_k] \cdot \frac{A_k}{C} \cong \frac{C}{A_k} \cdot \frac{\Delta q^2}{6} \cdot \frac{A_k}{C} = \frac{\Delta q^2}{6} \tag{37}$$

Comparing (37) with (22) shows that the MSE is equal in both uniform rectangular and circular distributions for rectangular quantizer due to equal size of cells in this quantizer.

(37) can be expressed in terms of number of bits for I and Q components B_r and full scale magnitude of the rectangular quantizer $2V_{s,r}$:

$$\overline{\varepsilon_{cr}^2} = \frac{2}{3}\frac{V_{s,r}^2}{2^{2B_r}} \tag{38}$$

1.3.2.2 SIGNAL POWER AND SQNR

The signal to quantization noise ratio (SQNR) can be calculated by dividing the average signal power (μ_c^2) to the average quantization noise power, $\overline{\varepsilon_{cr}^2}$. The average power of a signal with uniform circular distribution (μ_c^2) is calculated as:

$$\mu_c^2 = \int_0^{2\pi} \int_0^{a_c} r^2 \frac{r dr d\phi}{C} = \frac{a_c^2}{2} \tag{39}$$

where $C=\pi a_c^2$ is the total area of the circle in which signal is uniformly distributed.

From (39), SQNR of a rectangular quantizer for a signal with uniform circular distribution, ρ_{cr} is obtained:

$$\rho_{cr} = \frac{3}{2} \frac{\mu_c^2}{V_{s,r}^2} 2^{2B_r} = \frac{3}{4} \frac{a_c^2}{V_{s,r}^2} 2^{2B_r} \tag{40}$$

It is evident from (40) that SQNR linearly increase with signal power in this case . Comparing (40) and (25) reveals that for a given signal power, a signal with uniform circular distribution achieves the same SQNR as a signal with rectangular uniform distribution when they are quantized by a rectangular quantizer.

1.3.2.3 POLAR QUANTIZER

Similar to (26) and (28), the MSE of the polar quantizer within each quantization cell, $\overline{\varepsilon_{cp,k}}^2$ can be calculated similar to be:

$$\overline{\varepsilon_{cp,k}^2} = \frac{1}{12D_k} \left(r_k \Delta r^3 \Delta\phi + r_k^3 \Delta r \Delta\phi^3 \right) \tag{41}$$

Similar to (29), the MSE of the polar quantizer is calculated with R in (29) being replaced with C which denotes the area of the input circular distribution. We thus have:

$$\overline{\varepsilon_{cp}}^2 = \sum_k \overline{\varepsilon_{cp,k}^2} \cdot \frac{D_k}{C} = \frac{1}{C} \left(\Delta r^3 \Delta\phi \sum_k r_k + \Delta\phi^3 \Delta r \sum_k r_k^3 \right) \tag{42}$$

Assuming small Δr and $\Delta\phi$, Σr_k and Σr_k^3 are calculated similar to (30) and (31) to be:

$$\sum_k r_k \approx \frac{1}{\Delta r} \sum_{p=1}^{p=2^{B_p}} \frac{a_c^2}{2} = \frac{\pi a_c^2}{\Delta r \Delta \phi} \tag{43}$$

and

$$\sum_k r_k{}^3 \approx \frac{1}{\Delta r} \sum_{p=1}^{p=2^{B_p}} \frac{a_c^4}{4} = \frac{\pi a_c^4}{2 \Delta r \Delta \phi} \tag{44}$$

Plugging (45) and (44) in (42) and noting that $C = \pi a_c^2$, $\overline{\varepsilon_{cp}{}^2}$ is readily calculated:

$$\overline{\varepsilon_{cp}{}^2} = \frac{\Delta r^2}{12} + \frac{a_c^2 \Delta \phi^2}{24} \tag{45}$$

(45)is expressed in terms of polar quantizer full scale $V_{s,p}$ and number of bits for magnitude and phase parts, B_m, B_p, respectively:

$$\overline{\varepsilon_{cp}{}^2} = \frac{1}{12} \cdot \frac{V_{s,p}^2}{2^{2B_m}} + \frac{\pi^2}{6} \frac{a_c^2}{2^{2B_p}} = \frac{1}{12} \cdot \frac{V_{s,p}^2}{2^{2B_m}} + \frac{\pi^2}{3} \frac{\mu_c^2}{2^{2B_p}} \tag{46}$$

Comparing (46) with (32) shows that the MSE of the signal with uniform circular distribution grows with signal power (μ_c^2), similar to that of signal with rectangular distribution when both are quantized using a polar quantizer. However, one important advantage of using polar quantizer in case of uniform circular distribution is that smaller full-scale (by factor of $1/\sqrt{2}$) is required for polar quantizer compared to that in uniform rectangular distribution case, resulting in smaller MSE for uniform circular distribution.

It is seen from (46) that $\overline{\varepsilon_{cp}{}^2}$ has a term linearly increasing with signal power added to a constant term. From (39) and (46), SQNR of a polar quantizer for a signal with uniform circular distribution, ρ_{cp} is obtained:

$$\rho_{cp} = \frac{\mu_c^2}{\frac{1}{12} \cdot \frac{V_{s,p}^2}{2^{2B_m}} + \frac{\pi^2}{6} \frac{a_c^2}{2^{2B_p}}} = \frac{\mu_c^2}{\frac{1}{12} \cdot \frac{V_{s,p}^2}{2^{2B_m}} + \frac{\pi^2}{3} \frac{\mu_c^2}{2^{2B_p}}} \tag{47}$$

Shown in **Error! Reference source not found.** is the calculated SQNR of circular uniform complex signal for both rectangular and polar quantizers, ρ_{cr} and ρ_{cp}, respectively, indicating that the polar quantizer has higher SQNR than the rectangular quantizer for all average input magnitudes. To verify the analysis, the SQNR of both polar and rectangular quantizers are simulated and plotted on the same figure under various combinations of B_m/B_p quantization levels in the polar quantizer, assuming that the total number of quantization levels is fixed at $B_{tot} = 14$ bits. Similarly, for rectangular quantizer $B_r = B_{tot}/2 = 7$.
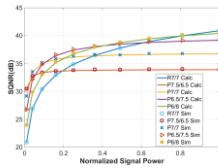
Figure 15 The simulated SQNR comparison between the 7Bi/7Bq uniform rectangular quantizer (R7.0/7.0) and various uniform polar quantizers (different M/P allocation) for Btot fixed at 14

Error! Reference source not found. compares the SQNR of a polar quantizer against that of a rectangular quantizer for signals with uniform circular distribution, when the number of phase bits runs from 4 to 10 under the assumption of constant number of bits ($B_m+B_p = 2B_r = 14$ in this case).

It is clear Figure 15 from that under optimal magnitude/phase bit allocation for polar quantizer, this quantizer achieves a higher SQNR compared to a rectangular quantizer, for low input signal powers when the input signal follows a uniform circular distribution. As the signal power increases the difference between maximum SQNR of the polar quantizer and that of the rectangular quantizer becomes smaller. Finally for very large input powers, the SQNR achieved by a rectangular quantizer becomes larger than that of a polar quantizer for signals with uniform circular distribution.

To compare the performance of rectangular and the polar quantizers for signals with uniform circular distribution, SQNR of both quantizers for a signal with uniform rectangular distribution is plotted in Figure 16, when B_p varies from 4 to 10. Figure 16 indicates that for signals with uniform circular distribution, polar quantizer achieves ~ 3dB higher SQNR than the rectangular quantizer for low power signals, which is attributed to the major contribution of phase quantization for low power signals. On the other hand, as the signals power increases the SQNR difference tends to decrease such that rectangular quantizer seem to demonstrate slightly higher SQNR for very high power signals, for which the polar quantizer SQNR is dominated by the magnitude resolution. Furthermore, we calculate the ratio of the SQNR associated with rectangular quantizer over that of the rectangular quantizer, α_r, noting that $V_{s,p} = V_{s,r} = V_s$. For this comparison, we also assume $B_m + B_p = 2B_r$. Therefore we have:

$$\alpha_c = \frac{\rho_{cr}}{\rho_{cp}} = \frac{\frac{3}{2}\mu_c^2/V_s^2 \cdot 2^{2B_r}}{\frac{1}{12} \cdot \frac{V_s^2}{2^{2(2B_r - B_p)}} + \frac{\pi^2}{3}\frac{\mu_c^2}{2^{2B_p}}} = \frac{2^{2(B_p - B_r)}}{8} + \frac{\pi^2}{2}\frac{\mu_c^2}{V_s^2} \, 2^{2(B_r - B_p)} \qquad 48$$
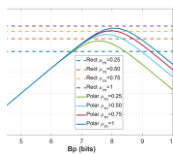
Figure 16 The SQNR comparison between the 7Bi/7Bq uniform rectangular and (14-Bp)/Bp polar quantizers for a signal with uniform rectangular distribution; μrn is the normalized signal power

To better illustrate this fact the SQNR ratio, α_c, is also plotted in Figure 17 which indicates that for a signal with uniform circular distribution, rectangular quantizer achieves higher SQNR compared to a polar quantizer for any signal power below the quantizer full-scale. Figure 17 indicates that for signals with uniform circular distribution, polar quantizer achieves higher SQNR than the rectangular quantizer ($\alpha_c < 0$dB), only for low signal powers. This is due to the dominancy of phase quantization for small signal magnitudes. For high power signals with uniform circular distribution, rectangular quantizer achieves slightly higher SQNR compared to polar quantizer.
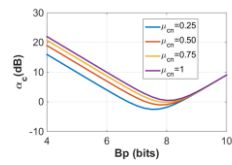
Figure 17 The SQNR ratio between the 7Bi/7Bq uniform rectangular and (14-Bp)/Bp polar quantizers for a signal with uniform circular distribution; μcn is the normalized signal power

1.3.3 Complex Gaussian distribution

Third, we consider complex Gaussian input distribution. In contrast with other two cases involving uniform distribution, there is always a finite probability that the received signal lies outside the quantizer full-scale which leads to quantizer overloading. Therefore, overloading error needs to be taken into account. For rectangular quantizer, we divide the complex plane into three regions, as shown in Figure 18, inside the quantizer (region I), only I or Q out of quantizer's range (region II), and both I and Q components outside quantizer's range (region III). We calculate the MSE for each region separately.

(a)   (b)
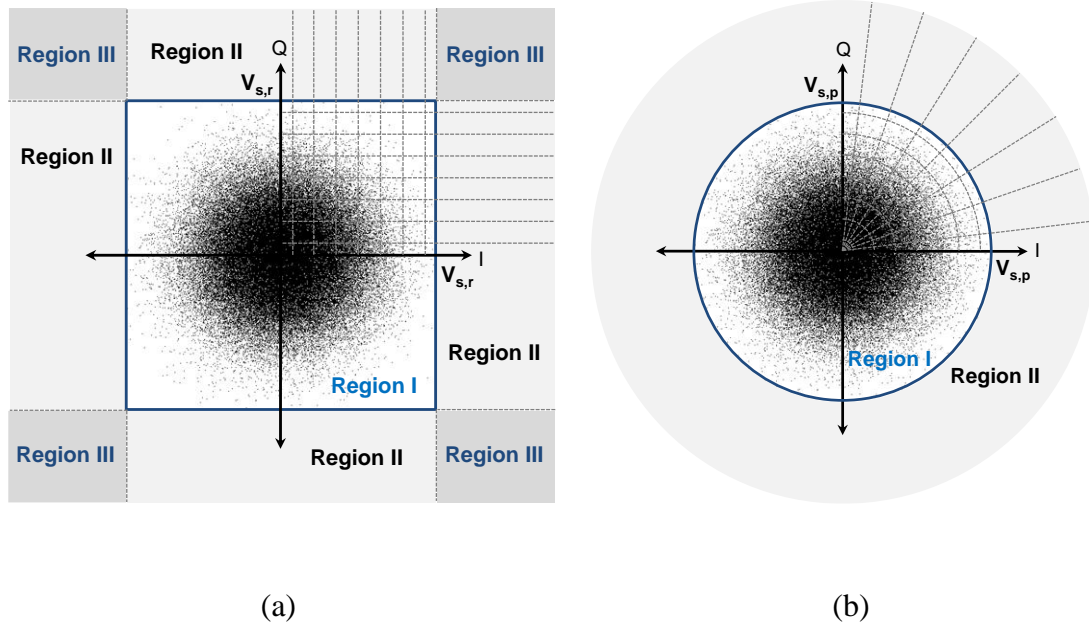
Figure 18 (a) Three regions for the rectangular quantizer to calculate the quantization errors. (b) Two regions for the polar quantizer to calculate the quantization errors.

1.3.3.1 RECTANGULAR QUANTIZER

Assuming small cells for the rectangular quantizer, we assume uniform distribution for the input

signal within each cell in region I. Thus, the MSE in this region $(\overline{\varepsilon_{Gr,I}{}^2})$ is:

$$\overline{\varepsilon_{Gr,I}{}^2} = \sum_k \frac{\Delta q^2}{6} \cdot P(Q_k) \tag{49}$$

where $P(Q_k)$ denotes the probability a the input signal falling into the boundaries of the kth

quantization cell and can be calculated as follow:

$$P(Q_k) = P\left(x_k - \frac{\Delta q}{2} < X < x_k + \frac{\Delta q}{2}\right) \cdot P\left(y_k - \frac{\Delta q}{2} < Y < y_k + \frac{\Delta q}{2}\right)$$

$$= \left[F\left(x_k + \frac{\Delta q}{2}\right) - F\left(x_k - \frac{\Delta q}{2}\right)\right] \cdot \left[F\left(y_k + \frac{\Delta q}{2}\right) - F\left(y_k - \frac{\Delta q}{2}\right)\right] \tag{50}$$

Assuming that the I and Q quantization intervals are small, (50) can be approximated by:

$$P(Q_k) \approx \Delta q^2 f(x_k) f(y_k) \tag{51}$$

where $F(.)$ and $f(.)$ are the cumulative distribution and probability density functions (CDF and

PDF), respectively. x_k and y_k denote coordinates of the center of each cell. Thus, (49) is expressed

$$\overline{\varepsilon_{r,I}{}^2} = \frac{1}{2\pi\sigma^2} \sum_k \sum_l \frac{\Delta q^4}{6} \cdot e^{\frac{-(x_k^2 + y_l^2)}{2\sigma^2}}$$

$$\approx \frac{\Delta q^2}{12\pi\sigma^2} \int\limits_{x,y=-V_s}^{x,y=V_s} e^{\frac{-(x^2 + y^2)}{2\sigma^2}} dx\, dy = \frac{\Delta q^2}{6} \operatorname{erf}^2\left(\frac{V_s}{\sqrt{2}\sigma}\right) \tag{52}$$

as:

If the signal lies in region II, either I or Q component experiences overloading. The value assigned

to this component will be the maximum value of the quantizer (V_s). In this region, the quantization

cells are narrow strip lines rather than squares (Figure 18 (a)). The MSE in this region is expressed as:

$$\overline{\varepsilon_{Gr,II}}^2 = 4 \cdot \frac{1}{2\pi\sigma^2} \sum_k \Delta q \, e^{\frac{-y_k^2}{2\sigma^2}} \int_{y_k-\frac{\Delta q}{2}}^{y_k+\frac{\Delta q}{2}} \int_{V_s}^{\infty} \{(x-V_s)^2 + (y-y_k)^2\} \cdot \frac{1}{\Delta q} \cdot e^{\frac{-x^2}{2\sigma^2}} dx dy \quad (53)$$

The two dimensional integration in (53), A, equals to:

$$A = \frac{1}{\Delta q} \int_{y_k-\frac{\Delta q}{2}}^{y_k+\frac{\Delta q}{2}} \int_{V_s}^{\infty} \{(x-V_s)^2 + (y-y_k)^2\} e^{\frac{-x^2}{2\sigma^2}} dx dy$$

$$(54)$$

$$= \sigma \sqrt{\frac{\pi}{2}} \left(1 - \text{erf}\left(\frac{V_s}{\sqrt{2}\sigma}\right)\right) \left(\sigma^2 + V_s^2 + \frac{\Delta q^2}{24}\right) - V_s \sigma^2 e^{\frac{-V_s^2}{2\sigma^2}}$$

Therefore, (53) is simplified to:

$$\overline{\varepsilon_{Gr,II}}^2 = \frac{2A}{\pi\sigma^2} \sum_k e^{\frac{-y_k^2}{2\sigma^2}} \Delta q \quad (55)$$

Replacing summation with integration in (55) we have:

$$\overline{\varepsilon_{Gr,II}}^2 = \frac{2A}{\pi\sigma^2} \int_{-V_s}^{V_s} e^{\frac{-y^2}{2\sigma^2}} dy = \frac{2\sqrt{2}A}{\sqrt{\pi}\sigma} \text{erf}\left(\frac{V_s}{\sqrt{2}\sigma}\right) \quad (56)$$

Finally, in region III, both I and Q components are outside the quantization range. The MSE is expressed as:

$$\overline{\varepsilon_{Gr,III}}^2 = \frac{4}{2\pi\sigma^2} \cdot \int_{V_s}^{\infty} \int_{V_s}^{\infty} [(x-V_s)^2 + (y-V_s)^2] \cdot e^{-\frac{x^2+y^2}{2\sigma^2}} dx dy \quad (57)$$

The two-dimensional integration in (57) is equal to:

$$B = \int\limits_{V_s}^{\infty} \int\limits_{V_s}^{\infty} [(x - V_s)^2 + (y - V_s)^2] \cdot e^{-\frac{x^2+y^2}{2\sigma^2}}\, dxdy$$

$$= \sigma \sqrt{\frac{\pi}{2}} \left(1 - \mathrm{erf}\left(\frac{V_s}{\sqrt{2}\sigma}\right)\right)(\sigma^2 + V_s^2) - V_s\sigma^2 e^{\frac{-V_s^2}{2\sigma^2}}$$

(58)

Using (58), (57) can be simplified to:

$$\overline{\varepsilon_{Gr,III}}^2 = \frac{4}{\sqrt{2\pi}\sigma} B \cdot \left(1 - \mathrm{erf}\left(\frac{V_s}{\sqrt{2}\sigma}\right)\right)$$

(59)

Finally, the MSE for the complex plane is expressed as:

$$\overline{\varepsilon_{Gr}}^2 = \overline{\varepsilon_{Gr,I}}^2 + \overline{\varepsilon_{Gr,II}}^2 + \overline{\varepsilon_{Gr,III}}^2$$

(60)

Plugging (52),(56) and (59) into (60), $\overline{\varepsilon_{Gr}}^2$ can be further simplified to:

$$\overline{\varepsilon_{Gr}}^2 = \frac{\Delta q^2}{12}\left(1 + \mathrm{erf}^2\left(\frac{V_s}{2\sigma}\right)\right) + 2(\sigma^2 + V_s^2)\left(1 - \mathrm{erf}\left(\frac{V_s}{2\sigma}\right)\right) - \frac{4}{\sqrt{2\pi}}\sigma V_s e^{-\frac{V_s^2}{2\sigma^2}}$$

(61)

1.3.3.2 SIGNAL POWER AND SQNR

The signal to quantization noise ratio (SQNR) can be calculated by dividing the average signal

power ($\mu_G{}^2$) to the average quantization noise power, $\overline{\varepsilon_{Gr}}^2$. The average power of a signal with

complex Gaussian distribution ($\mu_G{}^2$) is calculated as:

$$\mu_G^2 = \frac{1}{2\pi\sigma^2} \int\limits_{-\infty}^{+\infty} \int\limits_{-\infty}^{+\infty} (x^2 + y^2)e^{-\frac{x^2+y^2}{2\sigma^2}}\, dxdy = 2\sigma^2$$

62

From (61) and (62), the SQNR of a signal with complex Gaussian distribution ρ_{Gr} is obtained:

35

$$\rho_{Gr} = \frac{\mu_G^2}{\varepsilon_{Gr}^2}$$

$$= \frac{1}{\frac{\Delta q^2}{24\sigma^2}\left(1 + \mathrm{erf}^2\left(\frac{V_s}{2\sigma}\right)\right) + \left(1 + \frac{V_s^2}{\sigma^2}\right)\left(1 - \mathrm{erf}\left(\frac{V_s}{2\sigma}\right)\right) - \frac{2}{\sqrt{2\pi}\,\sigma}V_s\,e^{-\frac{V_s^2}{2\sigma^2}}} \qquad 63$$

1.3.3.3 POLAR QUANTIZER

For polar quantizer, we divide the complex plane into two regions, inside and outside the quantizer in Figure 18 (b). The MSE is separately calculated for each region. Similar to rectangular quantizer, the distribution of the input signal in each cell is assumed to be uniform. Using (41) and calculating D_k in terms of Δr and $\Delta\phi$, i.e., $D_k = r_k\Delta r\Delta\phi$, $\overline{\varepsilon_{Gp,I,k}^2}$ is be calculated to be:

$$\overline{\varepsilon_{Gp,I,k}^2} = \frac{1}{12}(\Delta r^2 + r_k^2\Delta\phi^2) \qquad (64)$$

The MSE inside the quantization region ($\overline{\varepsilon_{Gp,I}^2}$) is calculated as follows:

$$\overline{\varepsilon_{Gp,I}^2} = \sum_k \overline{\varepsilon_{Gp,I,k}^2} \cdot P(P_k) \qquad (65)$$

in which $P(P_k)$ is the probability of a signal following a complex Gaussian distribution, falling into the quantization cell P_k. Thus, for $P(P_k)$, we have:

$$P(P_k) = P\left(r_k - \frac{\Delta r}{2} < R < r_k + \frac{\Delta r}{2}\right) \cdot P\left(\phi_k - \frac{\Delta\phi}{2} < \Phi < \phi_k + \frac{\Delta\phi}{2}\right)$$
$$\approx \Delta r \cdot \Delta\phi \cdot \frac{1}{2\pi}f(r_k) \qquad (66)$$

where $f(r_k)$ denotes PDF of Rayleigh distribution for the magnitude signal. Moreover, $f(r)$ can be expressed as:

$$f(r) = \frac{r}{\sigma^2}e^{-\frac{r^2}{2\sigma^2}} \qquad (67)$$

By substituting $f(r_k)$ from (67) into (66), thus, $\overline{\varepsilon_{Gp,I}{}^2}$ is calculated as:

$$\overline{\varepsilon_{Gp,I}{}^2} = \frac{1}{12}\sum_k (\Delta r^2 + r_k^2\Delta\phi^2)\; f(r_k)\cdot\Delta r\cdot\frac{\Delta\phi}{2\pi} \tag{68}$$

r_k is much larger than Δr except for the case where the quantization level is close to origin. However, in that case, $f(r_k)$ is close to zero due to nature of Rayleigh distribution. Thus, the contribution of those cases to summation in (25) is negligible. Therefore, the denominator inside the summation is replaced by r_k. Assuming small cells, summation is replaced by integration:

$$\overline{\varepsilon_{Gp,I}{}^2} = \frac{1}{12}\,2^{B_p}\cdot\frac{\Delta\phi}{2\pi}\cdot\int_0^{V_s}(\Delta r^2 + r^2\Delta\phi^2)\cdot\frac{r}{\sigma^2}e^{-\frac{r^2}{2\sigma^2}}\,dr$$

$$= \frac{1}{12}\left[\Delta r^2\left(1 - e^{-\frac{V_s^2}{2\sigma^2}}\right) + 2\sigma^2\Delta\phi^2 - (2\sigma^2 + V_s^2)\Delta\phi^2\cdot e^{-\frac{V_s^2}{2\sigma^2}}\right] \tag{69}$$

For the outside region, region II, the magnitude quantizer will experience overloading, while the phase quantizer operation will not be affected. Therefore, the phase component of the signal is quantized as before. However, the quantized magnitude of the signal lying in this region will be the full-scale level of the magnitude quantizer, $V_{s,p}$. Therefore the MSE in this region can be obtained by calculating the average of the square of the distance between the signal and the quantizer boundary, which is expressed as:

$$\overline{\varepsilon_{Gp,II}{}^2} = \int_{-\frac{\Delta\phi}{2}}^{\frac{\Delta\phi}{2}}\int_{V_s}^{\infty}[r^2 + V_s^2 - 2rV_s\cos\theta]\cdot\frac{r}{\sigma^2}e^{\frac{-r^2}{2\sigma^2}}\cdot\frac{dr\,d\theta}{\Delta\phi}$$

$$= 2(\sigma^2 + V_s^2)e^{-\frac{V_s^2}{2\sigma^2}} - \left(\sqrt{2\pi}\sigma V_s\left(1 - \mathrm{erf}\left(\frac{V_s}{\sqrt{2}\sigma}\right)\right) + V_s^2 e^{-\frac{V_s^2}{2\sigma^2}}\right)\left(\frac{\sin\left(\frac{\Delta\phi}{2}\right)}{\frac{\Delta\phi}{2}}\right) \tag{70}$$

Assuming sufficiently high phase resolution, i.e. small $\Delta\phi$, $\sin(\Delta\phi/2)$ can be replaced by $\Delta\phi/2$. Thus, (70) can be approximated by:

$$\overline{\varepsilon_{Gp,II}^{2}} \cong (2\sigma^2 + V_s^2)e^{-\frac{V_s^2}{2\sigma^2}} - \sqrt{2\pi}\sigma V_S\left(1 - \text{erf}\left(\frac{V_s}{\sqrt{2}\sigma}\right)\right) \tag{71}$$

Similar to rectangular quantize, the MSE is calculated as the sum of MSE in each region.

$$\overline{\varepsilon_{Gp}}^{2} = \overline{\varepsilon_{Gp,I}}^{2} + \overline{\varepsilon_{Gp,II}}^{2} \tag{72}$$

Using (69) and (71), MSE in (72) is calculated to be:

$$\overline{\varepsilon_{Gp}}^{2} = (2\sigma^2 + V_s^2)e^{-\frac{V_s^2}{2\sigma^2}}(1 - \frac{\Delta\phi^2}{12}) + \frac{\Delta r^2}{12}\left(1 - e^{-\frac{V_s^2}{2\sigma^2}}\right) + \frac{\sigma^2\Delta\phi^2}{6}$$
$$- \sqrt{2\pi}\sigma V_S\left(1 - \text{erf}\left(\frac{V_s}{\sqrt{2}\sigma}\right)\right) \tag{73}$$

From (73) and (62), the SQNR of a polar quantizer for a signal with complex Gaussian distribution, ρ_{Gp} is obtained:

$$\rho_{Gp} = \frac{\mu_G^2}{\overline{\varepsilon_{Gp}}^{2}}$$

$$= \frac{1}{\left(1 + \frac{V_s^2}{2\sigma^2}\right)e^{-\frac{V_s^2}{2\sigma^2}}(1 - \frac{\Delta\phi^2}{12}) + \frac{\Delta r^2}{24\sigma^2}\left(1 - e^{-\frac{V_s^2}{2\sigma^2}}\right) + \frac{\Delta\phi^2}{12} - \frac{\sqrt{2\pi}V_S}{2\sigma}\left(1 - \text{erf}\left(\frac{V_s}{\sqrt{2}\sigma}\right)\right)} \tag{74}$$

Shown in Figure 19 is the calculated SQNR of complex Gaussin signal for both rectangular and polar quantizers, ρ_{Gr} and ρ_{Gp}, respectively, indicating that the polar quantizer has higher SQNR than the rectangular quantizer for all average input magnitudes. To verify the analysis, the SQNR of both polar and rectangular quantizers were simulated under various combinations of B_m/B_p quantization levels in the polar quantizer, assuming that the total number of quantization levels is fixed at $B_{tot} = 14$ bits. Similarly, for rectangular quantizer $B_r = B_{tot}/2 = 7$.
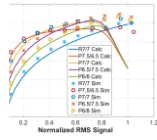
Figure 19 The simulated SQNR comparison between the $7B_i/7B_q$ uniform rectangular quantizer (R7.0/7.0) and various uniform polar quantizers (different M/P allocation) for B_{tot} fixed at 14 bits for complex Gaussian input PDF

It is evident from Figure 19 that SQNR starts to decrease as the signal RMS level exceeds a certain level. Quantizer overloading solely is responsible for this phenomenon. It is also seen that while, the theoretically calculated SQNR shows a good agreement with simulated SQNR for signals with low input power, it overestimates the SQNR degradation due to overloading. The calculated SQNR shows overloading at a lower input power. In addition, it shows a faster roll-off with respect to the input RMS voltage as a result of overloading effect.

Figure 20 compares the SQNR of a polar quantizer against that of a rectangular quantizer for signals with complex Gaussian distribution, when the number of phase bits runs from 4 to 10 under the assumption of constant total number of bits ($B_m+B_p = 2B_r = 14$ in this case). It is clear from Figure 20 that under optimal magnitude/phase bit allocation for polar quantizer, this quantizer achieves around 3- to 8dB higher SQNR compared to a rectangular quantizer for input signal following a complex Gaussian distribution, depending on the input signal power.
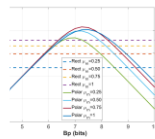
Figure 20 The SQNR comparison between the $7B_i/7B_q$ uniform rectangular and $(14\text{-}B_p)/B_p$ polar quantizers for a signal with uniform circular distribution; μ_{rn} is the normalized signal power

The difference between peak SQNR of polar quantizer (achieved under optimum B_m/B_p) and SQNR of the rectangular quantizer (ΔSQNR) is shown in Figure 21. It is clear from Figure 21 that under optimal magnitude/phase bit allocation for polar quantizer, this quantizer achieves a higher SQNR compared to a rectangular quantizer for input signal following a complex Gaussian distribution, especially when the power of the input signal is low. For large input powers, however, the overloading of the quantizer dominates the quantization error and degrades SQNR.
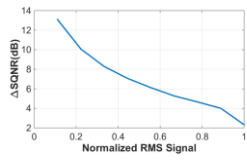
Figure 21 The SQNR improvement using the optimum B_m/B_p (B_m/B_p=14) polar quantizer with respect to the $7B_i/7B_q$ uniform rectangular for a signal with complex Gaussian distribution; ΔSQNR = $10\log_{10}(\rho_{Gp}/ \rho_{Gp})$ is the normalized signal power

Polar Quantization and Real Life Signals

In this chapter, we will discuss the system level impacts of polar signal processing and polar quantization on the performance parameters of a wireless link. The main performance parameters are symbol error rate (SER) and signal to quantization noise power ratio (SQNR).

This chapter is organized as follows. First, we compare the performance of polar and rectangular quantizers for signals with quadrature-amplitude (QAM) modulation. The discussion can be extended to orthogonal frequency division multiplexing (OFDM). The use of polar quantization in case of OFDM signal is particularly advantageous as a result of high peak to average power ratio (PAPR) that OFDM signal demonstrates.

1.4 QAM Signals and Polar Quantization

Quadrature amplitude (QAM) modulation is widely used modulation schemes in modern wireless communication systems due to their relatively high spectral efficiency (depending on the modulation order) and error resilience. At the transmitter side the constellation is set of clean dots on a grid on the complex plane. However, transmission of the QAM signal through the communication channel applies a random gain and phase shift to the signal, which can be represented by a complex number called channel gain. In general, channel gain can be frequency dependent. For a flat fading chancel, the channel gain statistics is governed by a complex Gaussian distribution. As a result of this random gain and phase shift the constellation is scaled and rotated at the receiver input. The receiver needs to compensate for this signal scaling and rotation by applying a proper rotation and scaling which needs to be the inverse of chancel scaling and rotation. This process is called chancel equalization. The equalization may need to be frequency dependent, for example to compensate for multipath fading, depending on the channel characteristics and frequency response.

One widely used approach to equalize the communication channel is to periodically send a signal known to the receiver, called pilot signal. The receiver is waiting for the pilot signal in a certain time slots within the communication interval. This interval begins with transmission and reception of the first pilot signal. Once the receiver detects the pilot signal, with a priori knowledge of the transmitted signal, it tries to find the channel response and apply the inverse transformation to the rest of the received signal, until the next pilot signal is detected. Nonetheless, since chancel equalization signal processing is done in digital domain, the received signals including the pilot signal appear unprocessed at the input of the quantizer. In other words, the receiver quantizer input sees a signal that has been distorted the random characteristics of the chancel gain. Therefore it is

43

essential to design the receiver front-end and quantizer such that it is able to accurately quantize the randomly distorted input signal. More importantly, if the receiver front-end and quantizer fail to accurately detect and quantize the pilot signal, the channel estimation will be erroneous, hence the entire received stream will be corrupted. In addition, due to presence of strong in-band and out-of-band interferes in the communication channel, the received signal cannot be always amplified to the quantizer full scale. Therefore, resolution of the quantizer is not always fully utilized. This demands the quantizers to introduce low quantization error, even for very small detected power. Another scenario of underutilized quantizer full scale is when the input signal itself has a high peak-to-average power ratio (PAPR). When the received signal has a high PAPR, the receiver automatic gain control (AGC) needs to reduce the gain such that the peak signal does not experience clipping. This means that the signal samples at average power are far below quantizer full-scale, demanding the quantizer to provide a large dynamic range. As discussed in the previous chapter, since polar quantizer inherently introduces less quantization error for lower input powers, it can potentially show higher SQNR for signals with high PAPR.

Considering the square QAM signals as an example, the dynamic range or PAPR of the signal increases as the modulation order increases. PAPR for different sizes of QAM signal is listed in Table 1QAM PAPR Comparison

Table 1QAM PAPR Comparison

QAM Size	4	16	64	256
PAPR(dB)	0	2.6	3.7	4.2
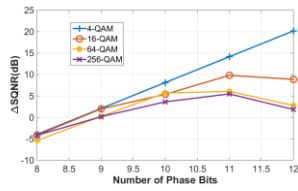
Figure 22 SQNR improvement of polar quantizer for M-QAM signals (ΔSQNR = SQNR$_{polar}$ − SQNR$_{rectangular}$) for several phase resolutions of polar quantizers ($B_m + B_p = 2B_r = 20$; B_p varies from 8 to 12)
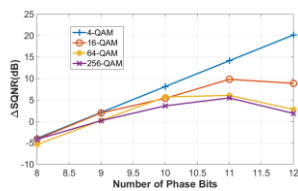
Figure 22 compares the SQNR improvement achieved by polar quantization for M-QAM signals received through a flat fading channel. The total number of bits for both polar and rectangular quantizer is assumed to be 20 ($B_m+B_p = 2B_r = 20$). The phase resolution, B_p, is varied from 8 to 12 bits. The SQNR difference, ΔSQNR (ΔSQNR = SQNR$_{polar}$ − SQNR$_{rectangular}$) is plotted versus B_p. The phase resolution plays more important role for lower size QAM signals. For example for 4-QAM signals, all the information is carried in the phase signal (constant magnitude). Therefore, the magnitude resolution has a minimum effect (only to correctly quantize the pilot signal for channel equalization), while the output SQNR is almost linearly proportional to the phase resolution.

Figure 23 compares the SQNR improvement achieved by polar quantization for M-QAM signals received through a flat fading channel. The total number of bits for both polar and rectangular quantizer is assumed to be constant B ($B_m+B_p = 2B_r = B$). The total number of bits, B, is varied from 14 to 20. The SQNR difference, ΔSQNR is plotted versus B. For each value of B, B_p is first swept and then chosen such that the polar quantizer achieves the maximum SQNR (optimum B_m/B_p). It is evident that the ΔSQNR is higher for smaller total number of bits. It indicates that while a rectangular quantizer can achieve almost similar performance as a polar quantizer for very high resolutions, a polar quantizer would demonstrate a superior SQNR performance at lower

resolutions where the SQNR of rectangular quantizer drops significantly, but that of polar quantizer only experiences slight degradation due to its efficient quantization mechanism.
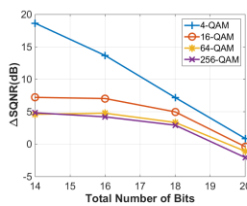
Figure 23 SQNR improvement of polar quantizer for M-QAM signals (ΔSQNR = SQNR$_{polar}$ − SQNR$_{rectangular}$) versus total number of bits, B (B$_m$ + B$_p$ = 2B$_r$ = B; B varies from 14 to 20).

Polar Receiver Architecture

1.5 System Architecture and Operation Principles

The proposed IF PRX is depicted in Figure 24. The IF down-conversion effectively eliminates the adjacent channel interference (ACI) and out-of-band blockers through the use of band-pass filters [16]. Phase and magnitude detection take place in IF domain, i.e. after the down-conversion, the input IF signal is separated in two paths, i.e., a magnitude quantizer path realized in voltage domain and a phase quantizer path in time domain. Magnitude quantization path obtains the magnitude information of the signal using an envelope detector, which extracts the envelope of the signal [17]. Afterwards, the variable gain amplifier (VGA) scales the signal to the full scale of the magnitude quantizer. The magnitude is then quantized, i.e., $A_{BB}(t) = A(t) + \hat{A}(t)$, where $A_{BB}(t)$ is the quantized magnitude and $\hat{A}(t)$ is the quantization error.
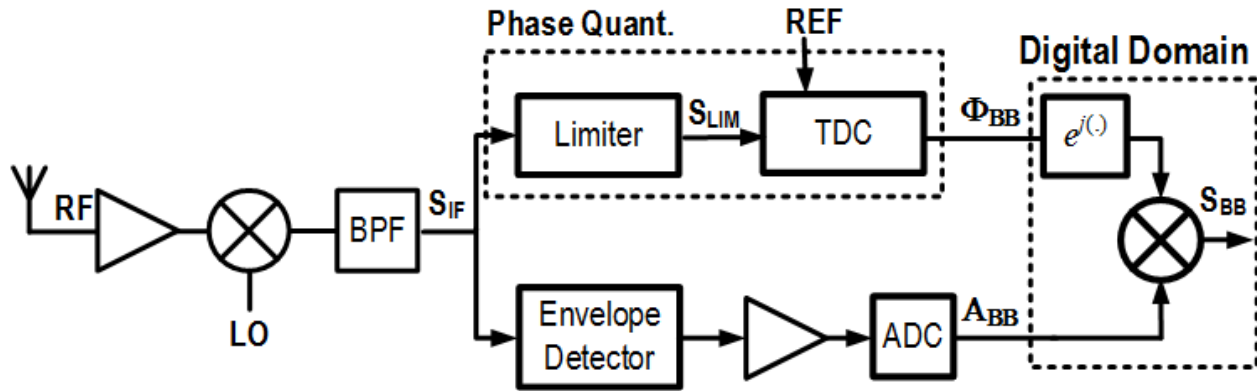
Figure 24 Polar quantizer architecture

There are many well-known methods for phase detection. The multiplier-based phase detector contains a sum and a difference frequency component. The difference frequency component represents the phase information, but the phase information is not linearly translated from the input

signal (among other drawbacks including limited dynamic range and sensitivity). On the other hand, the XOR-based phase detector has the well-known phase ambiguity problem [18].

To save area and reduce power consumption, a TDC-based phase quantizer is adopted, which realizes phase detection and quantization concurrently [19]-[24].

In phase quantizer path, the limiter first reshapes the IF signal (S_{IF}) into a constant magnitude square wave signal (S_{LIM}). This signal is then compared against a reference signal (*REF*), toggling at a frequency equal to IF, to determine its phase information. The phase difference between S_{LIM} and *REF* is extracted by measuring the time difference between rising edges of these two signals (T_{DIFF}) using TDC. The digital output of TDC is used to reconstruct the phase of the IF signal. Details of the TDC operation will be explained in the next Section. The phase quantizer output Φ_{BB}(t) is expressed as $\Phi_{BB}(t) = \phi(t) + \hat{\phi}(t)$, where $\hat{\phi}(t)$ is phase quantization error.

After being quantized in both paths, the signals are reconstructed digitally to obtain the complex baseband data, i.e.

$$S_{BB}(t) = \left(A(t) - \hat{A}(t)\right) e^{j\left(\phi(t) - \hat{\phi}(t)\right)} \tag{75}$$

1.6 System Design and Implementation Considerations

This section discusses the implementation aspects and system-level design of the PRX. Since the magnitude information is obtained using a conventional envelope detector and magnitude quantizer [25], only the phase detection method is discussed in details.

1.6.1 Phase Quantizer

A time-to-digital convertor (TDC) is used to detect and directly quantize the phase of the IF signal. In the phase quantization path the limiter first removes the magnitude information by generating

S_{LIM}. Then, TDC measures the phase by comparing the (S_{LIM}) against a known reference toggling at IF frequency.

Shown in Figure 25 is a conventional delay-based TDC [19]. It uses delay cells and synchronized registers to detect the time difference between S_{LIM} and delayed versions of *REF*. The propagation delay of each cell determines the quantization error, and hence, resolution.
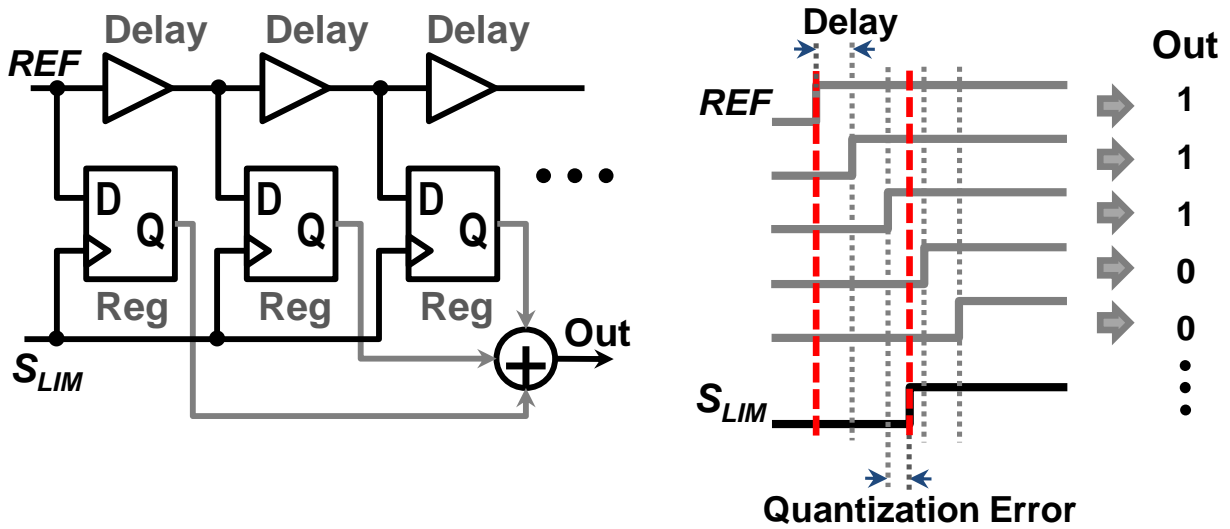
Figure 25 A conventional delay chain TDC and its operation

Assuming delay steps of t_s for the TDC shown in Figure 25, the phase resolution in phase quantization operation of the TDC is readily calculated to be:

$$\Delta\phi = 2\pi \frac{t_s}{T_{IF}} = 2\pi f_{IF} t_s$$

(76)

It is evident from (76) that the delay steps and/or f_{IF} should be minimized for maximum phase resolution (minimum $\Delta\phi$). Minimizing f_{IF}, however, imposes stringent challenges on the design of the image reject filter. The minimum propagation delay, τ_D, on the other hand, is determined by the technology, which sets an upper bound on the maximum achievable phase resolution using this TDC architecture. This maximum achievable resolution using delay based ring TDC topology is

increased with technology scaling [19]. One drawback of this topology, however, is the large number of delay stages, N, required to cover the entire period of the IF signal, T_{IF}. In other words, T_{IF} in this design needs to be greater the accumulated delay of all N delay stages, but smaller than the delay of N+1 delay stages, or otherwise the whole IF period is not covered.

$$N\tau_d < T_{IF} < (N+1)\tau_D \qquad (77)$$

As evident from (77), once the number of delay stages is determined, T_{IF} can only vary within a very limited range of only one time resolution step. This would significantly reduce the flexibility of the system in choice of the IF frequency.

Another candidate for implementing TDC is the ring oscillator-based TDC and is shown in
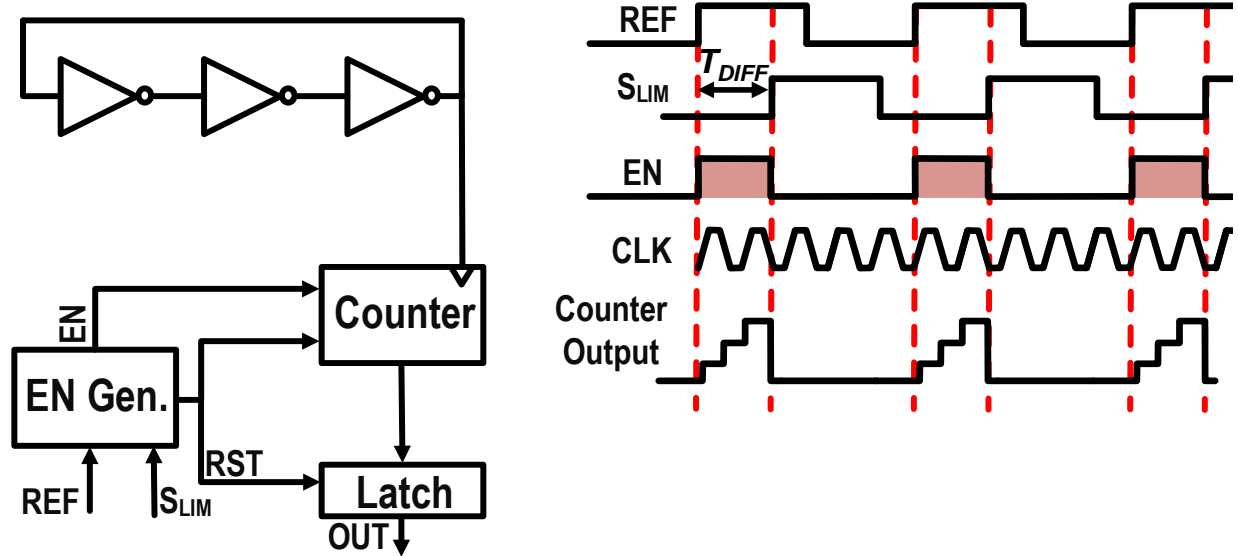
Figure 26 [19]. Enable generator circuitry enables the counter employed in TDC between rising edges of S_{LIM} and REF. The counter count the number of zero crossings of locally generated high frequency clock signal during this period, T_{DIFF}.

The resolution depends on the clock frequency (f_{CLK}) which is generated by a ring oscillator. The maximum achievable f_{CLK} using inverter based ring oscillator topology depends on minimum

propagation delay; hence it is also increased with technology scaling [19]. Thus this topology is also amenable to technology scaling. The amenability to technology scaling also brings forth yet another advantage, namely, lower power consumption.

Assuming N inverters in the ring oscillator, $f_{CLK} = 1/(2N\tau_D)$, where τ_D is the propagation delay. The counter counts the zero crossings of the clock signal. Noting the existence of two zero crossings per clock cycle, the minimum measurable time step, t_s is equal to:

$$t_s = \frac{1}{2f_{CLK}} = N\tau_D \tag{78}$$
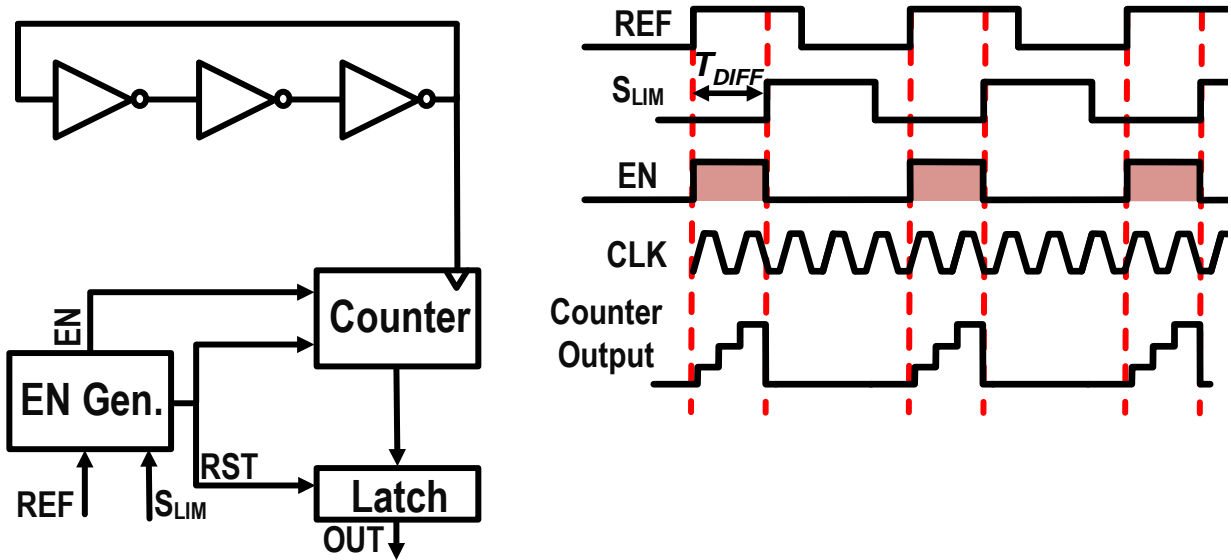
Figure 26 Ring oscillator-based TDC. Counter counts the zeros crossing of clock signal generated by the ring oscillator between rising edges of REF.

(78) indicates that in order to minimize t_s, the number of stages in the ring oscillator should be chosen as low as possible. This leads to achieving the maximum oscillation frequency. Nonetheless, the number stages cannot be chosen lower than 3 in a ring oscillator. Therefore the minimum time step in this topology is at least three times higher than that of the delay-based TDC, thus the phase resolution is three times lower.

Interestingly, different phases of the clock signal already existing at outputs of different stages of the ring oscillator can be used to improve the phase resolution by reducing t_s. In order to increase the number of zero crossings different phases of clock signal are used to drive several counters in parallel, as shown in Figure 27. Clock signals fed to the counters are equally delayed with respect
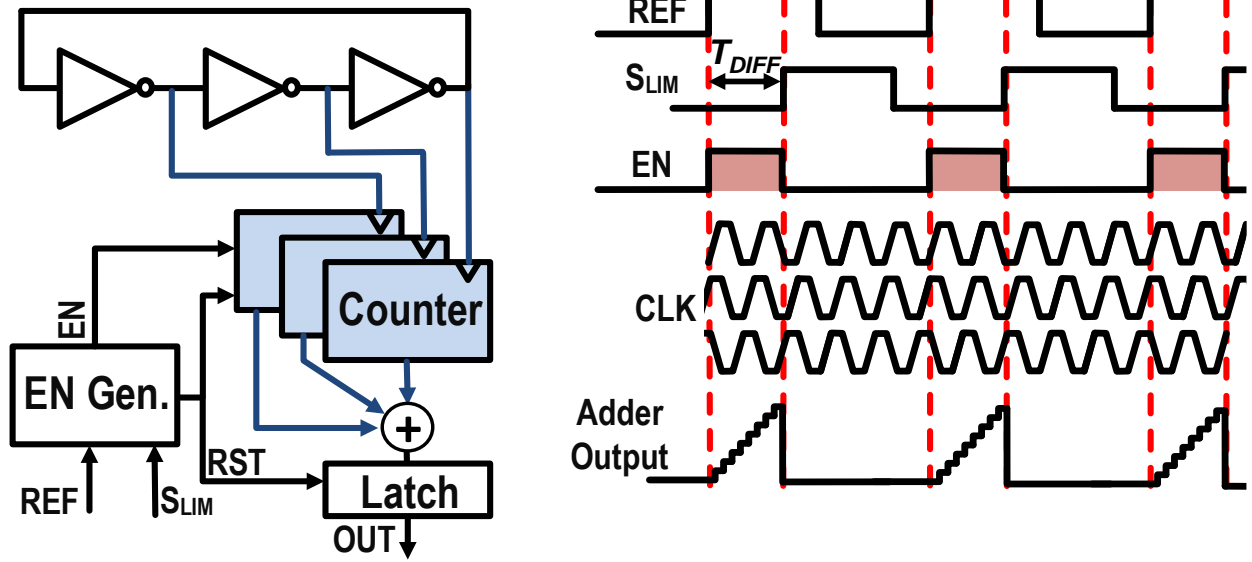
Figure 27 Multiphase ring oscillator based TDC. Each counter counts the zeros crossing of a certain phase of clock signal during T_{DIFF}. The outputs of the counters are added together.

to each other so that more number of zero crossings occurs during T_{DIFF} compared to using one counter and one clock signal. The counters' output are added together to form a digital data, essentially with higher resolution. Moreover, since N taps of the ring oscillator are used to feed N counters with delayed clocks$(\text{delay} = n\tau_D \; n = 0, ..., N - 1)$, t_s would be N time smaller in this case:

$$t_s = \frac{1}{2Nf_{CLK}} = \tau_D \tag{79}$$

(79) suggests that the multi-phase ring oscillator based TDC can achieve the same time resolution as the delay based TDC, while only using as low as only three delay stages. Moreover, the choice of IF frequency is now decoupled from the number of delay stages. If f_{IF}, needs to be changed from

the nominal value after the implementation for any reason, the only required adjustment would be to set the reference frequency according to f_{IF}.

If phase detection takes place in one cycle of S_{IF}, the minimum phase step $\Delta\phi$ is thus equal to:

$$\Delta\phi = 2\pi t_s f_{IF} = 2\pi \cdot \frac{\tau_D}{T_{IF}} \tag{80}$$

To alleviate this tight trade-off between f_{IF} and phase resolution, using the averaging method by employing a gated ring oscillator (GRO) based TDC provides a distinct advantage [19]. More precisely, as shown in Figure 28, the averaging allows the counters to measure the phase over one symbol period of the baseband signal (T_{BB}). The TDC enables the oscillator during T_{DIFF} in each IF cycle when the counters are enabled. Otherwise, it stores the phase of the ring oscillator. Thus, the phase is effectively measured over T_{BB}. Therefore, $\Delta\phi$ will be:

$$\Delta\phi = 2\pi t_s f_{IF} = 2\pi \cdot \frac{\tau_D}{T_{BB}} \tag{81}$$
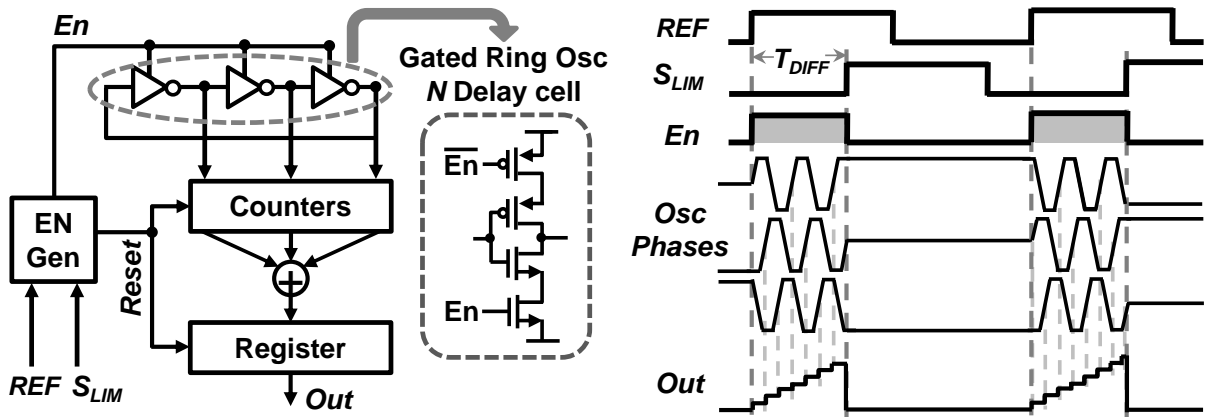
Figure 28 Gated ring oscillator (GRO) TDC with averaging method for phase detection.

However, the finite reset time associated with counters leads to the TDC failure in detecting the phase differences close to 360°. This is simply because the counters will not have enough time to

be correctly reset and the constituent latches may stay in metastable state, therefore the output of

the counters for next IF cycle will not be valid (see Figure 29). Same phenomenon happen when
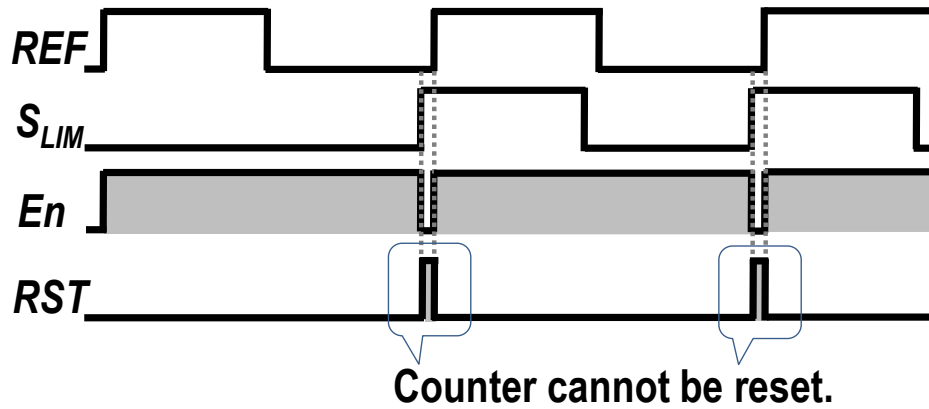
Figure 29 Narrow RST pulses for phase difference of REF and S_{LIM} close to 360°.

the phase difference is close to zero where the enable pulse is very short. This leads to a big dead

zone in TDC output.

To address this issue, two separate paths are used to quantize the phase; namely, one for quantizing

the phase when it lies within the range $0° - 180°$, and one for the range $180° - 360°$ ((a)
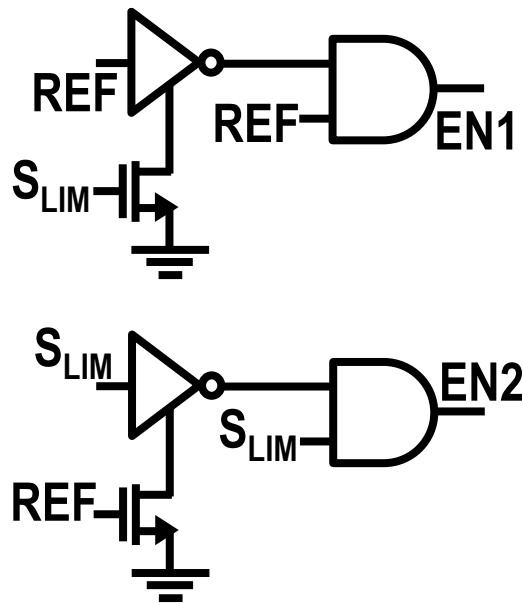
(b)

Figure 30 (a)). One path is sensitive to the rising edge of *REF* while the other one operates based on the falling edge of reference. At any given instance of time, only one path is enabled and it will remain in the enable state for as long as at most $T_{IF}/2$. Therefore, the reset time for counters in each path is prolonged by at least $T_{IF}/2$.

To enable the path corresponding to each range, the TDC needs to distinguish between leading and lagging rising edges of S_{LIM} with respect to that of *REF*. This feature is realized in the TDC using the enable generator (Enable Gen) circuitry, which generates enable signals en_1 and en_2, each for one path. An indicator signal S_{IND} is generated based on en_1, en_2 and *REF* to determine the corresponding phase range. The multiplexer selects and passes the output of the active path to the quantizer output based on S_{IND} status (Figure 30).
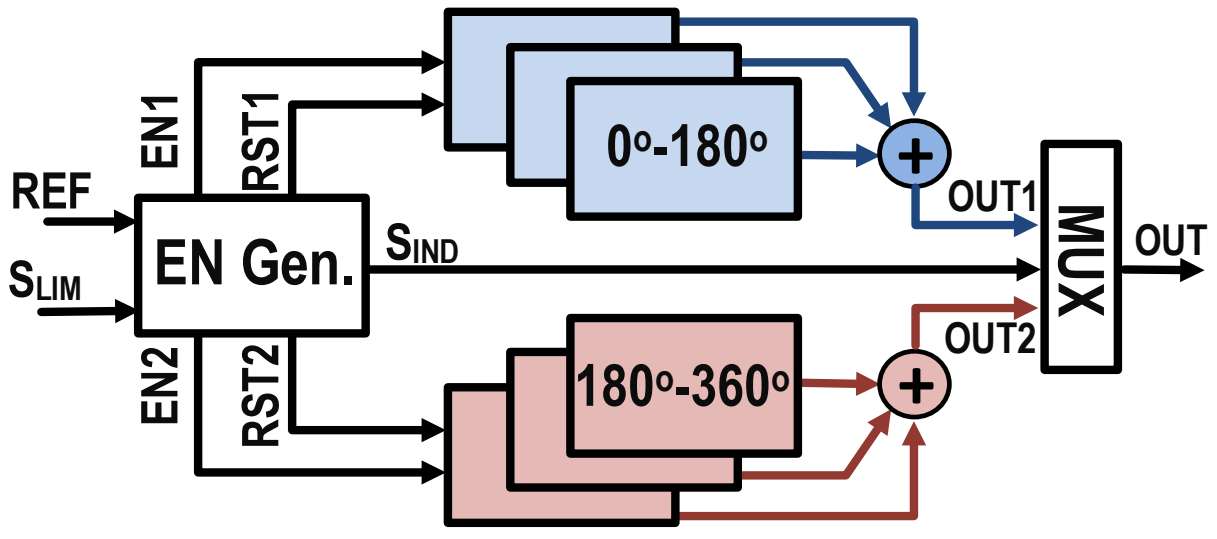
(a)
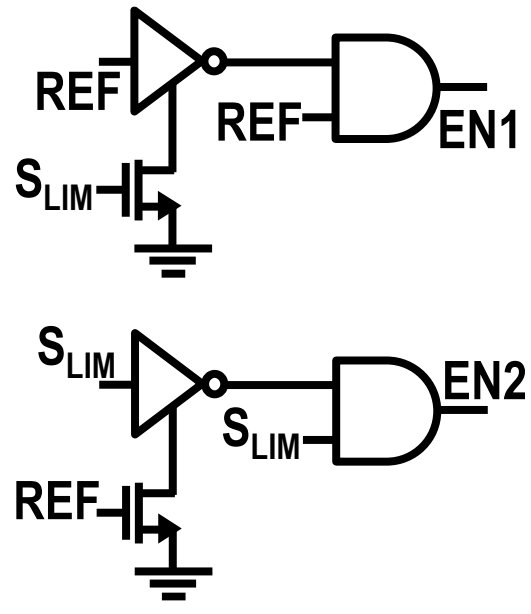
(b)

Figure 30 (a) Dual path TDC. One path (0°-180°) detects time differences between REF and S_{LIM} less than half period and the other path (180°-360°) detect time differences greater than half period of REF and S_{LIM} (b)Enable generator circuitry

Nonetheless, distinguishing between leading and lagging imposes a delay as high as T_{IF} in detecting the correct phase range, simply because the TDC has to wait for the next rising edge of S_{LIM} to recognize the transition from $0° - 180°$ to $180° - 360°$ or vice versa. Thus, whenever there is one such phase transition in S_{LIM}, the quantized phase will only be valid in the next IF cycle. This implies that the output of the TDC in the first IF cycle should be disregarded. Therefore, there should be at least two phase measurements per each symbol period so that the first one can be ignored and the result of the second one is taken as the valid phase quantized phase. As a result, T_{IF} should be lower than half the symbol period (T_{BB}). This constraint, imposed by the TDC implementation, sets a lower bound for f_{IF}.

Disregarding the first cycle of S_{LIM} and *REF* phase difference quantization (measurement of T_{DIFF}) results in resolution degradation, as averaging takes place over smaller number of IF cycles. This issue becomes less significant as f_{IF} increases. In this case, the longest time period that TDC can measure (i.e., TDC full scale) is equal to $T_{BB}-T_{IF}$. Therefore, based on (81), $\Delta\phi$ is readily calculated to be:

$$\Delta\phi = 2\pi \cdot \frac{\tau_D}{T_{BB} - T_{IF}} \tag{82}$$

As indicated clearly in (82), the resolution is improved if τ_D is decreased. However, τ_D is ultimately hard-limited by the f_{max} of the transistor in a given technology. For example, the minimum τ_D in 130nm CMOS process used in this design is 35ps, leading to a 9.45-bit resolution for $1/(T_{BB}-T_{IF})$ = 40MHz. To further improve the resolution beyond limitation imposed by the technology, a new idea is explored to increase the number of clock zero crossings in one cycle of the IF signal. Increasing the number of zero crossings essentially requires access to more phases of the clock signal. Increasing the number of stages to increases the number of clock phases,

however, proportionally reduces the clock frequency and therefore fails to improve the phase resolution. If two ring oscillators are coupled and a certain phase shift is enforced between them, the number of different phases can potentially increase without sacrificing clock frequency. For example for two *N*=3 stage ring oscillator in which two consecutive zero crossing are 60 degrees apart, enforcing 90 degrees phase difference doubles the symmetric zero crossings each 30 degrees spaced, as shown in Figure 31.
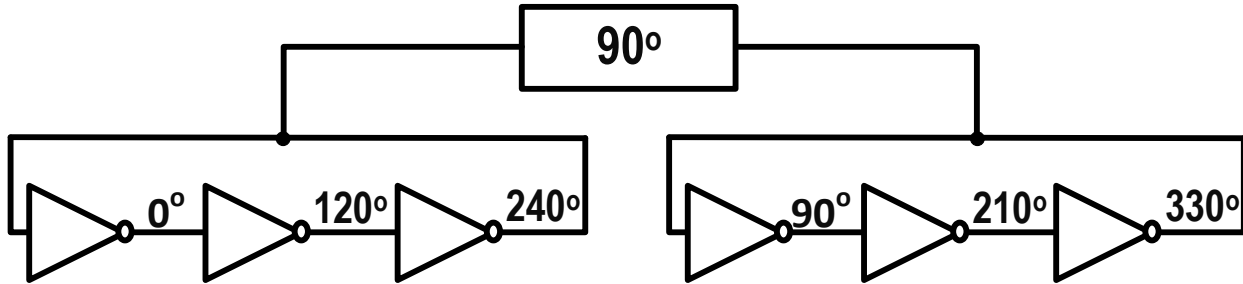
Figure 31 Two coupled N=3 stage ring oscillators. The coupling mechanism enforces 90° phase difference between the ring oscillators

The two identical 3-stage ring oscillators of Figure 31 are coupled using a quadrature cross coupled pair shown in Figure 33. The two coupled cross coupled pair forming quadrature cross coupled pairs forces a 90° phase difference between two oscillators. Thus, the total number of zero crossings of the clock signals is increased from 6 to 12 in one clock cycle. In other words, the temporal spacing between two consecutive zero crossing is decreased from τ_D to $\tau_D/2$, resulting in two-fold phase resolution improvement, i.e.,

$$\Delta\phi = \pi \cdot \frac{\tau_D}{T_{BB} - T_{IF}} \tag{83}$$

Dummy loads are placed at the drain nodes of cross coupled pairs to avoid any asymmetry in phases of the clock signals at different tap point of the two oscillators.
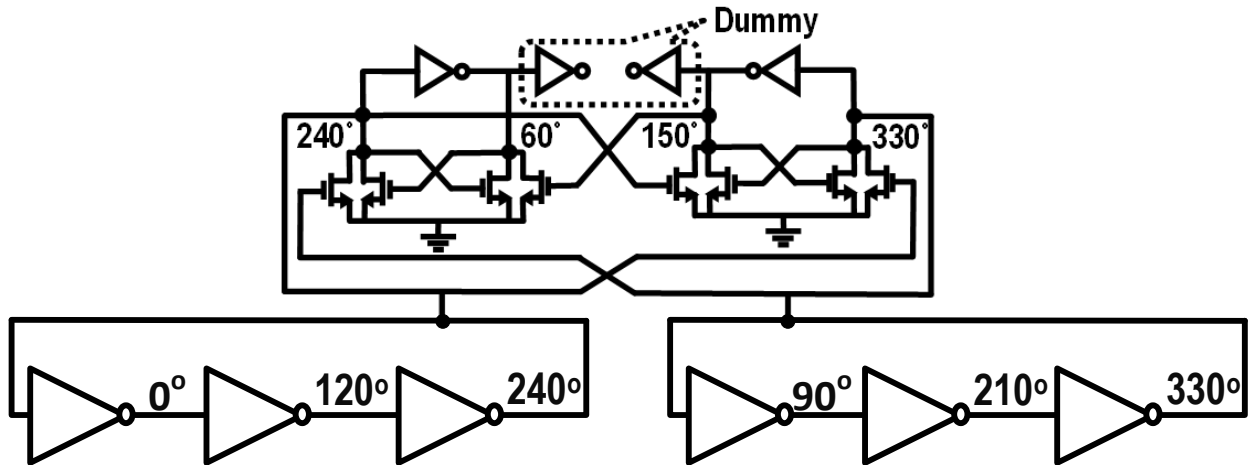
Figure 33 Two coupled N=3 stage ring oscillators are coupled through a quadrature oscillator which enforces 90º phase difference between the ring oscillators

The complete block diagram of the TDC based phase quantizer consisting of the quadrature coupled ring oscillators as clock generators and the dual path 6 phase parallel counters, the adders and the enable generator circuit is shown in Figure 32.
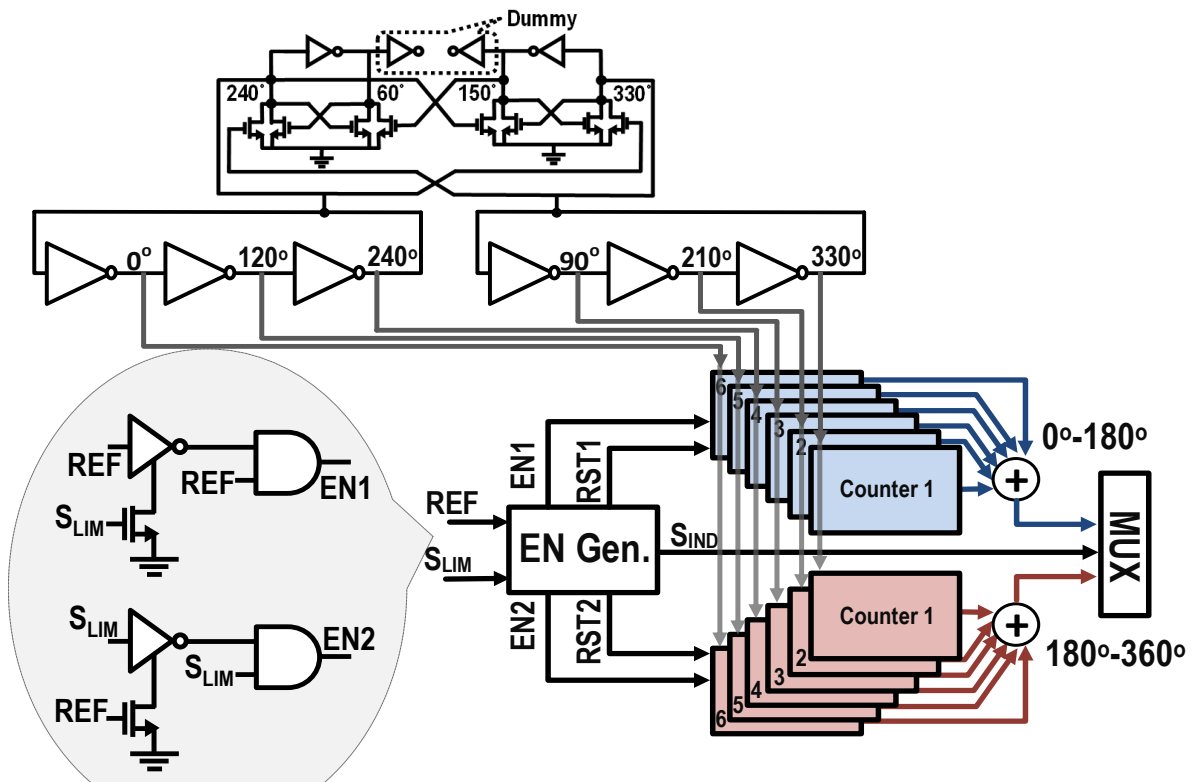
Figure 32 TDC based phase quantizer block diagram

60

1.6.2   Phase Quantizer Timing Diagram

The timing diagram of the phase quantizer is shown in Figure 34. Distinguishing between leading and lagging signals causes a delay in the TDC response. In other words as shown in the figure if there is a phase transition from leading to lagging in S_{LIM}, since the rising edge of S_{LIM} is already gone at rising edge of reference, the TDC has to wait for next cycle of *REF* signal to be able to detect that. Therefore the corresponding enable signal is not generated. The corresponding path is not activated and the appropriate output will not be generated. Thus, phase detection has to wait until next REF cycle.
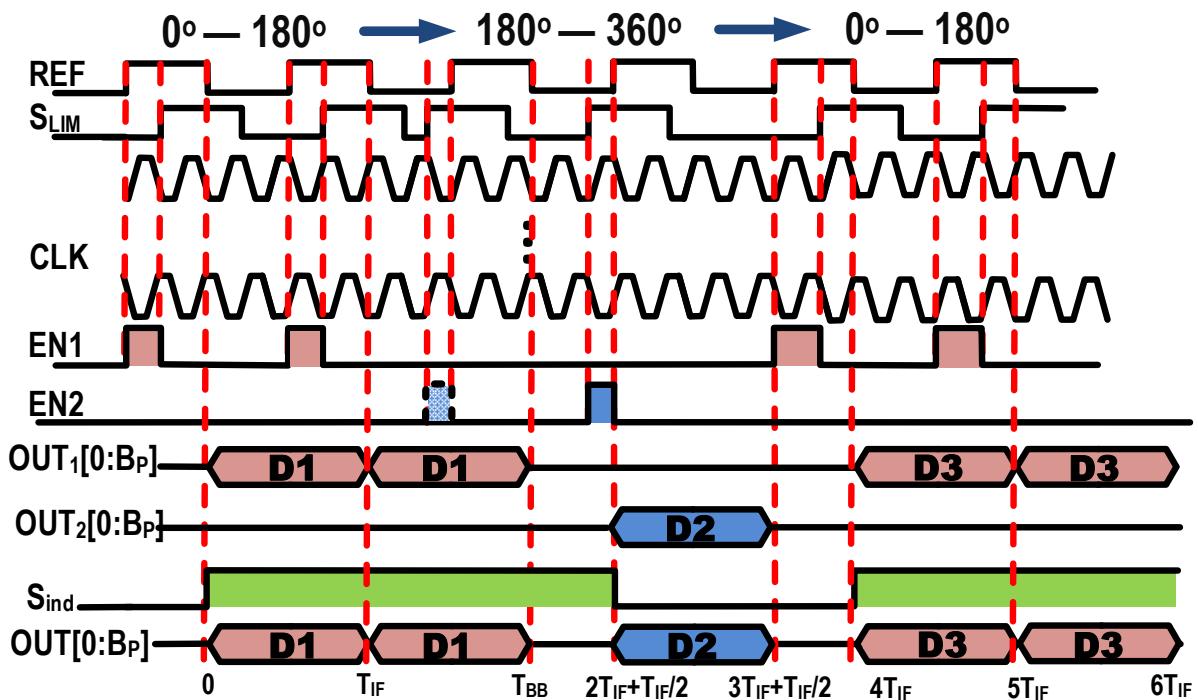
Figure 34 TDC based phase quantizers timing diagram

Signal Filtering and Bandwidth Expansion in Polar Receiver

1.7 Blocker Tolerance

Both magnitude and phase detection are nonlinear operations. Therefore, any undesired signal, S_B (e.g. adjacent channel or interferer) accompanying S_{IF} at the quantizer input, will distort the detected phase and magnitude which could not be filtered out in analog domain after the detection. In other words, the detected phase and magnitude would correspond to the base-band equivalent of the sum signal at the quantizer input, $S_B + S_{IF}$. The band-pass filter at the input of the quantizer is therefore necessary to sufficiently attenuate interferes, before entering the quantizer. Nevertheless, due to limited quality factor of on-chip components, a sharp on-chip band-pass filter at the IF frequency is a power hungry and/or area hungry. As a result, the phase and magnitude components will be corrupted if no further processing is taken place. Thus there should be a mechanism implemented to recover the desired signal from the distorted quantized signal.

Assuming that the quantizer input consists of the desired IF signal, S_{IF} and the interferer S_B the input signal seen by the quantizer, S_T, is:

$$S_T(t) = S_{IF}(t) + S_B(t) = S_T(t)$$

$$= Re\{e^{j2\pi f_{IF}t}(A_{IF}(t)e^{j\phi_{IF}(t)} + A_B(t)e^{j(2\pi\Delta ft + \phi_B(t))})\}$$

$$(84)$$

where Δf is the frequency offset of the interferer signal from channel center frequency or f_{IF}, Therefore, we can assume that S_T is the actual quantizer input and our task is to faithfully reconstruct S_T after quantization. More specifically, we can consider S_T as a varying envelope, varying phase signal, modulated by the carrier frequency, f_{IF}. Therefore, it can be expressed in terms of its instantaneous magnitude and phase and its carrier frequency:

$$S_T(t) = Re\{A_T(t)e^{j(2\pi f_{IF}t + \phi_T(t))}\} \tag{85}$$

Thus the base-band equivalent of S_T, $S_{T,BB}$, is expressed as:

$$S_{T,BB}(t) = A_T(t)e^{j\phi_T(t)} = A_{IF}(t)e^{j\phi_{IF}(t)} + A_B(t)e^{j(2\pi\Delta ft + \phi_B(t))} \tag{86}$$

The quantized magnitude and phase, $\widehat{A_T}$ and $\widehat{\phi_T}$ can be used to reconstruct $S_{T,BB}$ in digital domain.

$$\widehat{S_{T,BB}}(t) = \widehat{A_T}(t)e^{j\widehat{\phi_T}(t)} = S_{T,BB}(t) + n_q(t)$$

$$= A_{IF}(t)e^{j\phi_{IF}(t)} + A_B(t)e^{j(2\pi\Delta ft + \phi_B(t))} + n_q(t) \tag{87}$$

Where n_q(t) is the quantization noise. The reconstructed version, $\widehat{S_{T,BB}}$, assuming sufficiently high

SQNR, thus contain a component at the offset frequency Δf, which can be removed using digital

filtering. Consequently, in order to guarantee successful removal of the interferers, the polar

quantizer should be able to accurately quantize the summation of the desired and all the

interference signals at its input. Therefore, all the interferers that are not removed by the band-pass

filter before the quantizer, should fall into the quantizer bandwidth. In other words, the quantizer

bandwidth should be wide enough to be able to successfully quantize all the strong frequency

components of its input to facilitate interference rejection through digital filtering.

1.8 Bandwidth Expansion

Phase and magnitude detection as nonlinear operations also introduce another aspect worthy of

consideration, the bandwidth expansion. In nonlinear operations, frequency domain information is

not preserved, meaning that not all the frequency components at the output can be mapped to a

corresponding frequency component at the input. This usually translates to higher occupied

bandwidth of the output signal compared to the input signal, known as bandwidth expansion. The

problem of signal bandwidth expansion has been noticed and studied in the context of polar

transmitters [26]. Figure 35 shows the power spectral density (PSD) of a complex base-band 16-

QAM signal passed through a raised cosine pulse-shaping filter and PSD of its magnitude and phase components. It is evident that the phase signal occupies a much wider bandwidth compared to the complex base-band signal. The magnitude component also shows high power spikes at harmonics of the symbol rate which are due to inherently non-zero average of this signal.
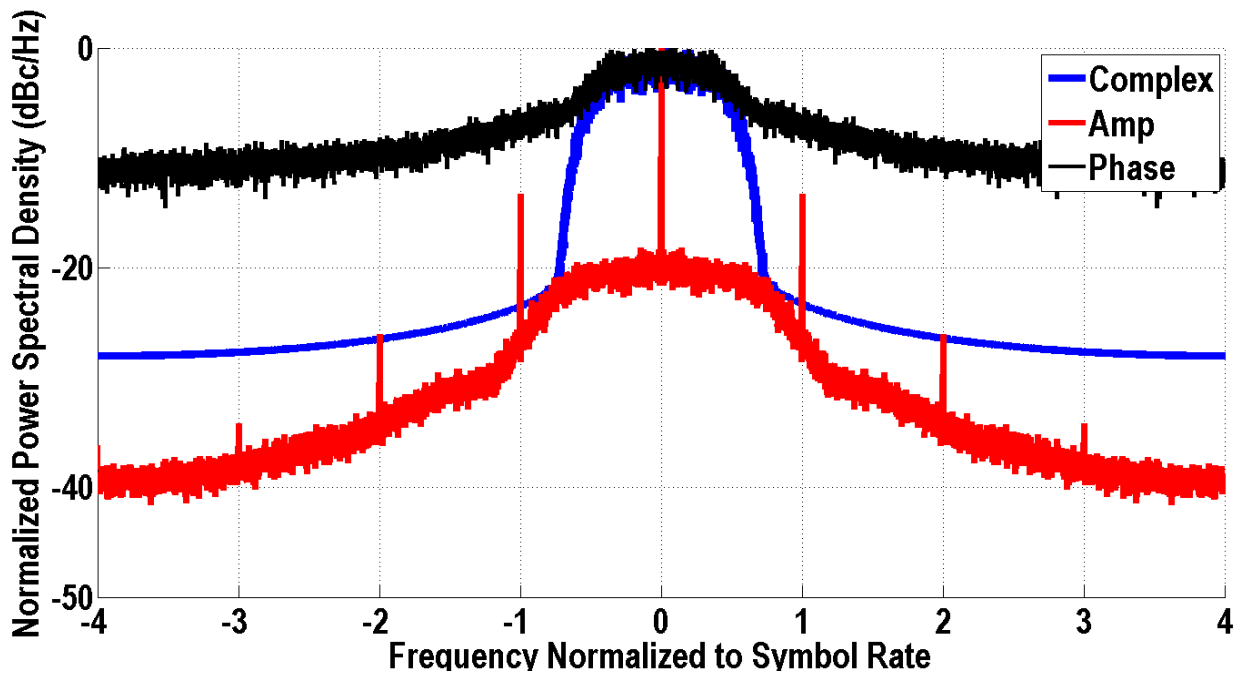
Figure 35 Power spectral density for a 16-QAM complex base-band signal and its phase and magnitude components. Raised cosine filter is used for pulse shaping

Similarly, the bandwidth expansion of the phase signal is also expected, since the operation of the limiter as a block that removes the magnitude variation is to introduce very sharp transitions to a smoothly varying signal, which essentially creates high amount of higher frequency components. Figure 36 shows the PSD of the limiter output. Comparing it against the PSD of the phase signal reveals that they occupy almost the same bandwidth. Since the core TDC building blocks, including the high speed counters and the enable generator circuit operate based on fast digital switches, the TDC is not the bandwidth bottleneck of the phase quantizer. As long as the gates are fast enough to generate valid enable signals and the counters can respond to the corresponding

set/reset signals, the TDC can assume to be broad band circuit. Therefore, the main bandwidth limiting block that is the limiter which is usually implemented as cascade of high gain buffers, which consequently trades bandwidth with gain and power. The gain of the limiter also determines the zero-crossing accuracy of its output.
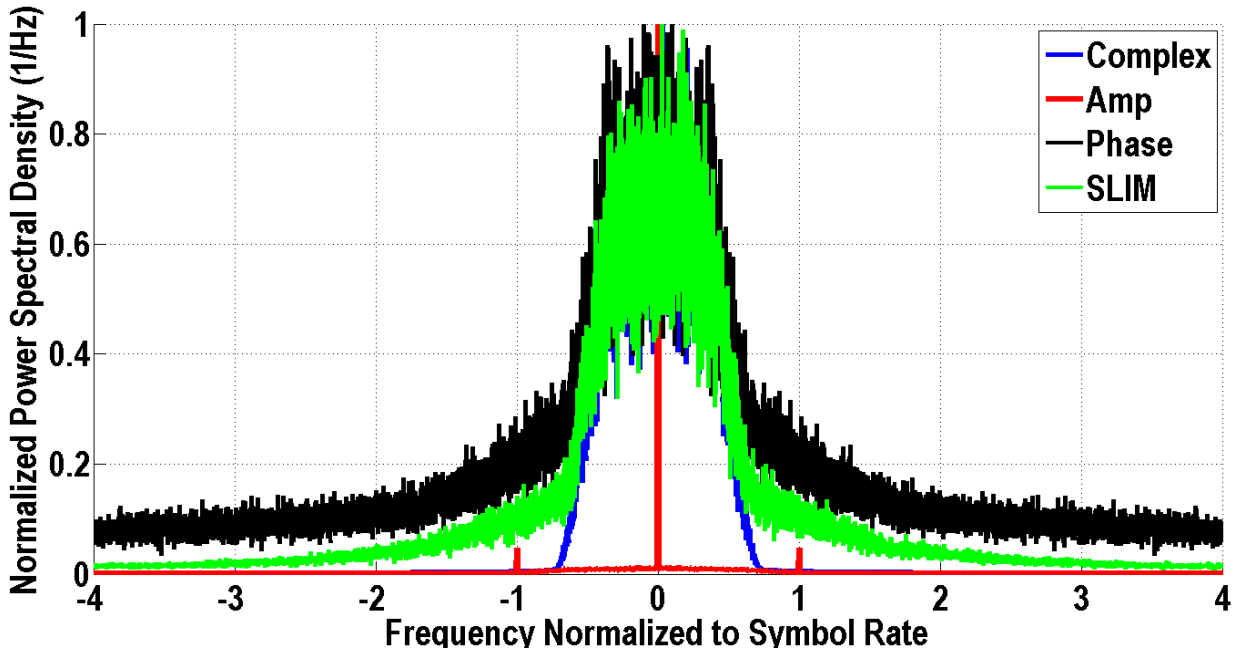
Figure 36 Power spectral density for a 16-QAM complex base-band signal and its phase and magnitude components. Raised cosine filter is used for pulse shaping. The phase signal shows same behavior as the limiter output, S_{LIM}, in the frequency domain

Polar Quantizer Implementation and Measurement Results

Shown in Figure 37 is the proposed phase quantizer fabricated in a 130nm standard CMOS process. The TDC phase detection fails to instantaneously generate the correct enable signals when the phase is suddenly changed from $0° - 180°$ to $180° - 360°$ or vice versa. Therefore, the phase quantizer needs at least two cycles of IF signal for correct phase detection of one baseband symbol, as explained in chapter 4. As a result, T_{IF} must, at most, be half T_{BB}. To best satisfy the aforementioned trade-offs regarding the location of f_{IF}, the IF and reference frequencies are chosen to be 40MHz for channel bandwidth of 20MHz (i.e. TX DAC rate of 20Msps) in this prototype design.
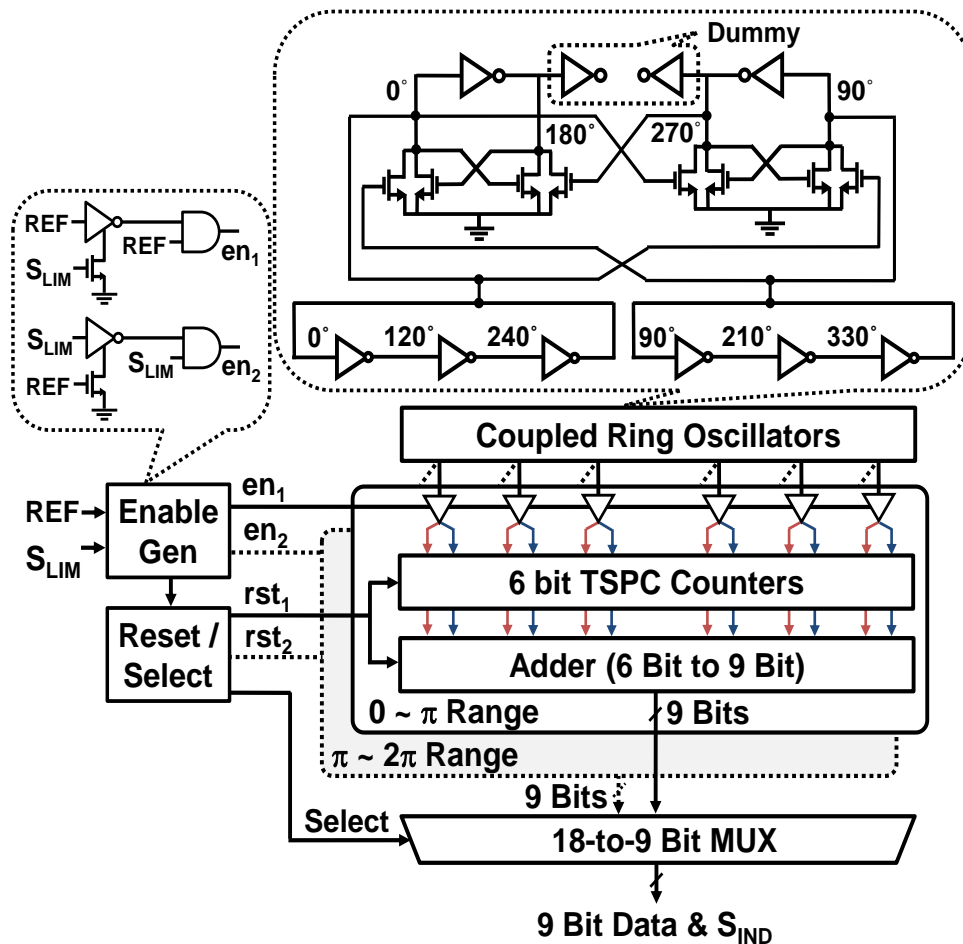
Figure 37 Phase quantizer architecture implemented in 130nm CMOS

Figure 38 shows the measurement setup. I and Q baseband data are fed to a vector signal generator (VSG) to generate the signal S_{IF}. S_{IF} and *REF* are then connected to the PCB for qunatizer measurements. The quantized phase, magnitude, I and Q signals are all passed through buffers to drive a 4 channel 16 bit logic analyzer to capture the baseband data. f_{CLK} is first measured with the counters implemented in TDC. The two ring oscillators, coupled through the quadrature cross coupled pair, oscillate at 3.41GHz, resulting in a 0.35° phase step with *N*=6 different clock phases as explained in Chapter 4. Instead of a clock zero-crossing counter (i.e. double edge counter) two complementary counters, one rising-edge and one falling-edge counter, are used for each clock phase at each TDC quantization path. Thus, 12 counters are used for each phase range. 6 bit rising- and falling-edge true single-phase clocking counters (TSPC) are employed to achieve high operation speed to be able to use a high clock frequency. The outputs of 12 counters in each phase range path are added together using a 9 bit tree-adder shown in Figure 37. The measured f_{CLK} is then used to convert the TDC output to quantized phase of S_{LIM}.
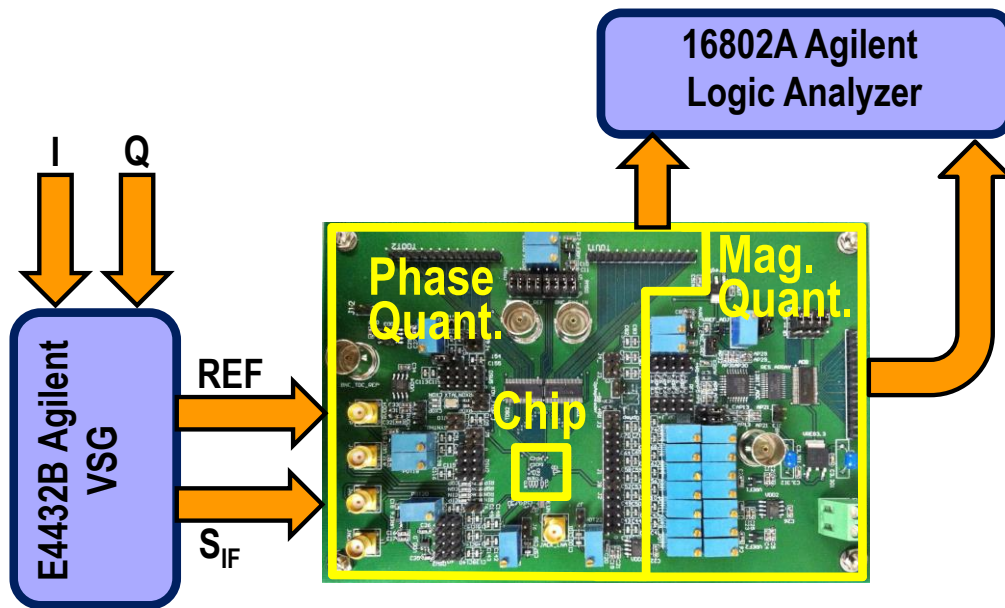
Figure 38 Polar quantizer measurement setup

The measured TDC transfer curves are shown in Figure 39. Two Agilent arbitrary waveform generators (AWGs) were synchronized together and used as *REF* and S_{IF}. The phase difference was controlled using the delay adjustment option available on the AWGs. The phase difference between REF and S_{IF} is swept from 0° to 360° and the output code word is measured by Agilent logic analyzer 16802A. As the phase difference varies from 0° to 180°, the TDC output code-word increases from 0 to 512 and then it decreases to 0 as the phase difference increases toward 360°. S_{IND} plays the role of the 10th bit of the quantizer. Due to finite gate propagation delay, the enable generator fails to generate narrow-width *en1* and *en2* pulses, when rising edges of *REF* and S_{LIM} come close to each other. This leads to a finite dead-zone in the vicinity of 0° (360°) which is measured to be 3.96° and is depicted in Figure 39.

INL and DNL measurements of the TDC, obtained from average value of several repetitions of the TDC output measurements, are shown in Figure 40. Both INL and DNL are within ±1 LSB. The dead-zone is removed from INL/DNL curves.
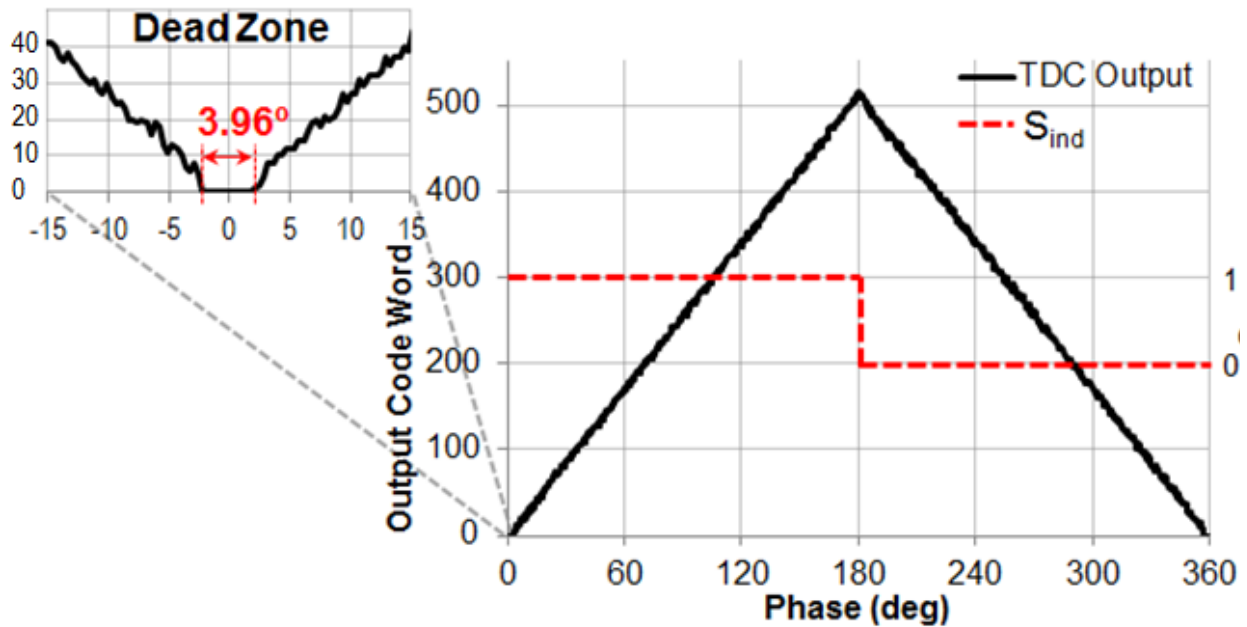
Figure 39 Measured TDC transfer curve
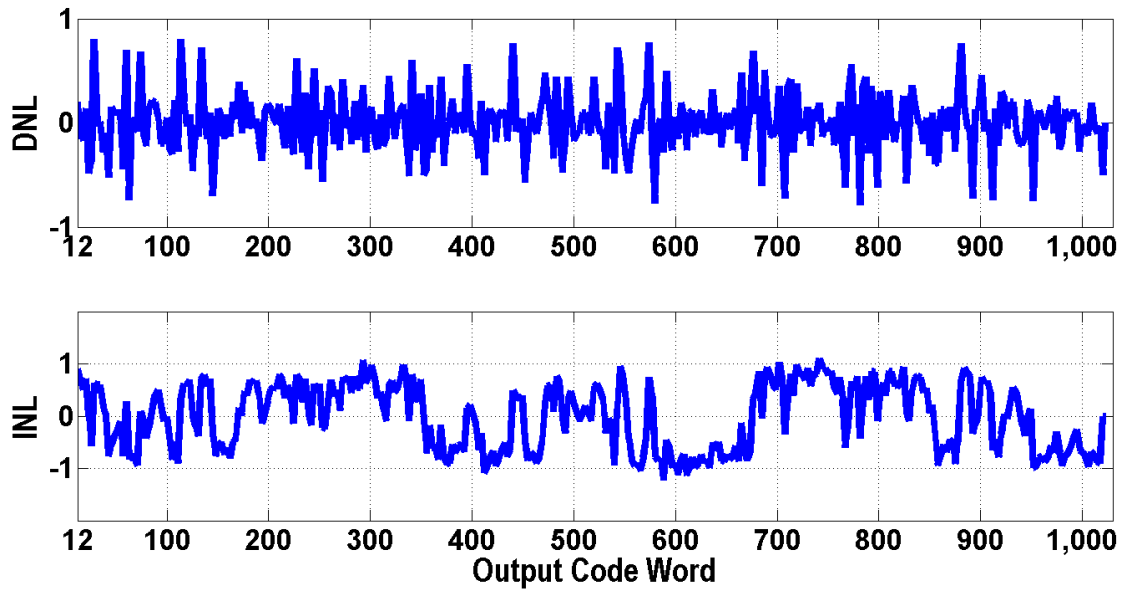
Figure 40 Measured INL and DNL

Figure 41 verifies the capability of TDC in tracking abrupt changes in phase of S_{LIM}. A pseudo-BPSK signal is generated as the input to the TDC and its phase was altered by 180° every 50ns using a (VSG). As is evident in Figure 41 (c) and (d), the measured quantized phase exactly follows the input phase. It indicates that TDC can track the phase of the received baseband signals as fast as 20Msps.

To measure the delay mismatch between phase and magnitude quantization paths a gated tone is applied to both magnitude and phase quantizers (at IF port) to measure the delay in response time of each. The on-off switching frequency f_{meas} of the applied tone is chosen low enough (2.5MHz) to accommodate settling time for both paths so as to accurately measure the delay difference. From measurement, the magnitude quantizer exhibits 49ns longer response time compared to the phase quantizer. This delay mismatch is then calibrated by pairing each measured magnitude sample with the delayed data of the phase quantizer stored in the logic analyzer. When it comes to practical implementation of the polar RX, one way to calibrate the delay mismatch between magnitude and

phase quantization paths is by toggling a delayed version of *REF* to the IF port at a certain frequency f_{meas}. f_{meas} should be low enough to allow both paths to settle so as to capture the delay between them. A DSP can store the data of faster path in a memory to use it later when the data from the slower path becomes available. The required memory size in terms of number of samples depends on the delay mismatch measured by the DSP.
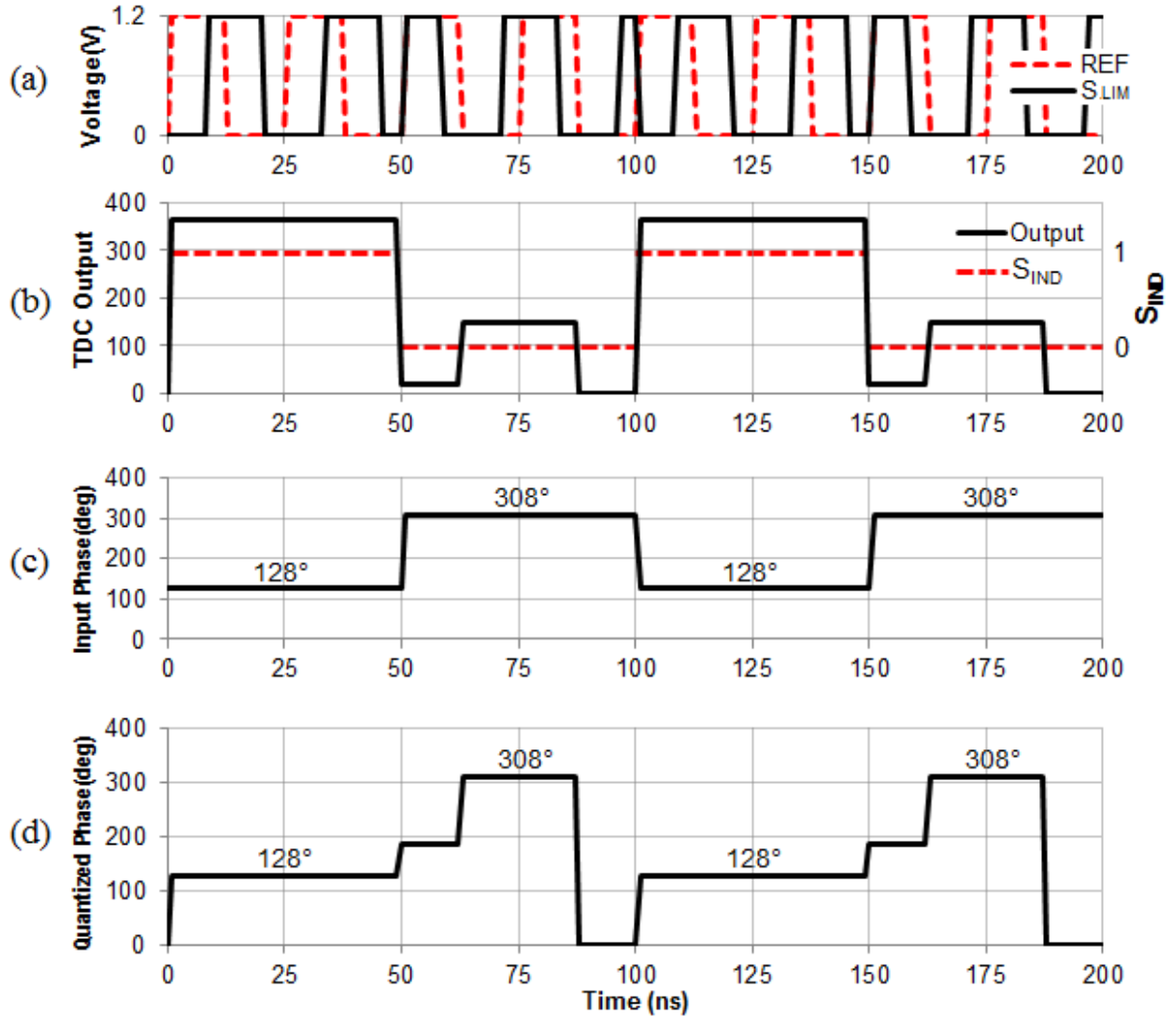
Figure 41 Operation of phase quantizer under pseudo-BPSK signal. (a) S_{LIM} and S_{REF}, (b) measured TDC outputs, (c) input phase and (d) measured quantized output phase.

To experimentally prove polar quantizer's superior performance compared to the rectangular counterpart, a zero mean complex Gaussian PDF with average input magnitude varying from 10- to 250-mV is generated and modulated with a 40MHz signal using VSG. The TDC-based phase quantizer detects and quantizes the phase part. An ADL5511 envelope detector and an ADC12040 12 bit ADC are used to detect the magnitude part. I and Q baseband data are fed to two similar ADCs for rectangular quantization in baseband, similar to a Cartesian direct conversion receiver.
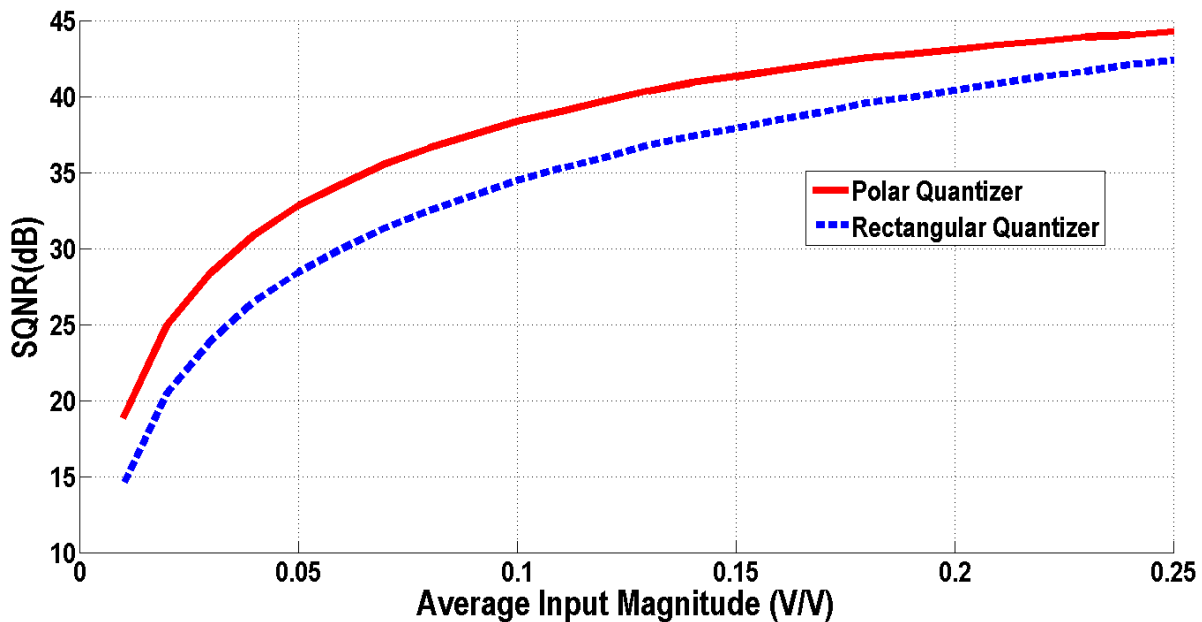
Figure 42 Measured SQNR vs. input average magnitude for polar and rectangular quantizers under complex Gaussian input PDF. 10 bit resolution for I/Q and magnitude/phase parts

Polar quantizer outperforms the rectangular quantizer, especially for smaller input average magnitudes, where SQNR is inherently low. As shown in Figure 42, polar quantizer achieves 2- to 5-dB higher SQNR compared to rectangular quantizer.

In another experiment shown in Figure 43, to verify the higher SQNR of polar quantizer compared to rectangular quantizer for Gaussian signals, a Gaussian signal was generated and then fed to both polar and rectangular quantizers. While the phase resolution was determined by TDC and

fixed at 10 bits the ADC resolution which determines the I, Q and magnitude resolution was

changed from 9 to 11. The measurements showed 5.5dB SQNR improvement for 10 bit ADC

resolution. Also the SQNR of a 10bit phase/11 bit amplitude quantizer is seen to be almost equal

to that of an 11 bit I/ 11 bit Q quantizers, indicating that one bit of resolution can be saved to save

more power, while achieving same SQNR performance as the rectangular quantizer. It is also

evident that the polar quantizer is much less sensitive to ADC resolution. It only shows 2 db

variation when magnitude reslolution changes from 9 to 11 bits. This feasure can be used in

adaptive resolution adjustment for low power applications.
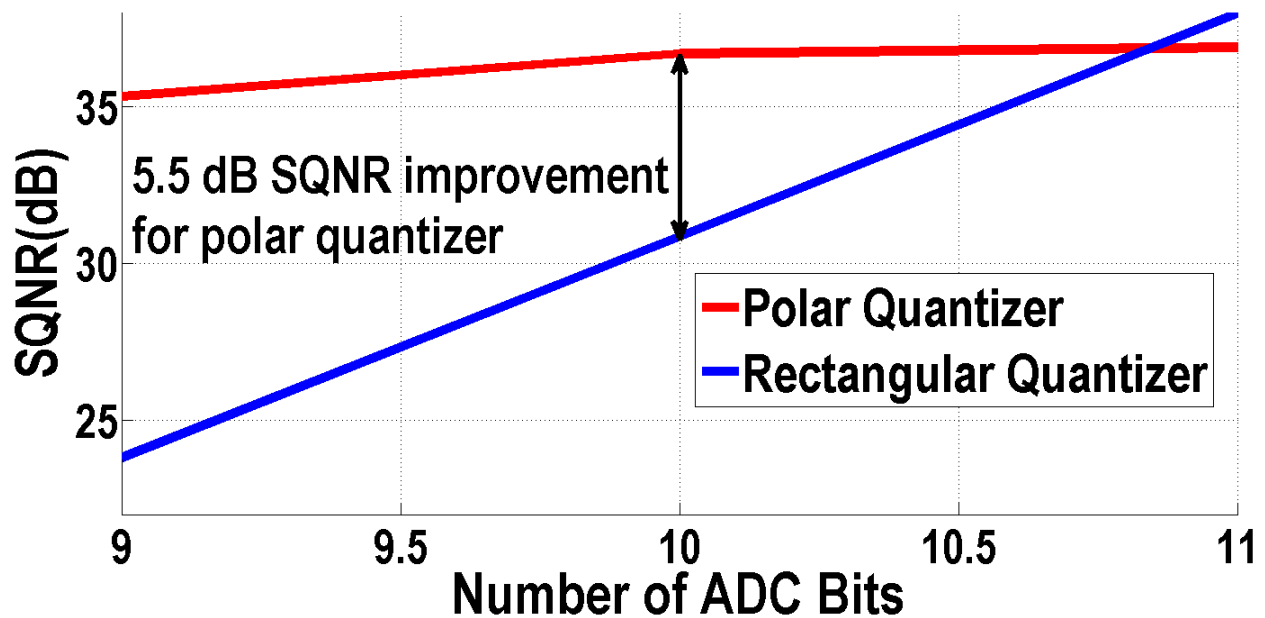
Figure 43 Polar and rectangular SQNR comparison; $B_p = 10$, $B_m = B_r = B$; I/Q and magnitude resolution B varies from 9 to 11 bits.

Table 2 shows a comparison between this work and state of the art. To compare this work with

prior work two figure of merits (FoM) are used. One is the conventional data convertor FoM which

is sampling rate times quantization levels divided by DC power consumption in dB scale. Using

this FoM this work is better than all previous works except ones at lower technology nodes.

$$FoM_1 = \frac{f_s 2^{B_p}}{P_{DC}} \qquad (88)$$

To capture the effect of employed technology we define another FoM which is the first FoM divided by ft of the technology.

$$FoM_2 = \frac{FoM_1}{f_T} \qquad (89)$$

With this FoM our TDC is better than all previous works except [21] in which a similar approach of using counters has been employed but the problem of limited dynamic range due to insufficient reset time of counters has not been resolved.

Table 2 TDC Performance Comparison

References	[21]	[27]	[28]	[29]	[30]	[31]	This work
Resolution (bit)	11	8	7	9	7	5	10
Sampling Rate (Msps)	50	50	50	10	180	26	40
Power (mW)	10.5	4.3	1.7	3	3.6	6.9	7.3
CMOS Tech. (nm)	130	130	65	90	90	90	130
FoM$_1$	80	70	71	65	76	42	75
FoM$_2$	37	27	20	18	30	-5	32

Finally, the power consumption of phase quantizer depends on the phase difference between S_{REF} and S_{LIM}, and changes from 3.9 to 10.75mW. The die photograph of phase quantizer and board photograph of polar quantizer are shown in Figure 44 (a) and (b).
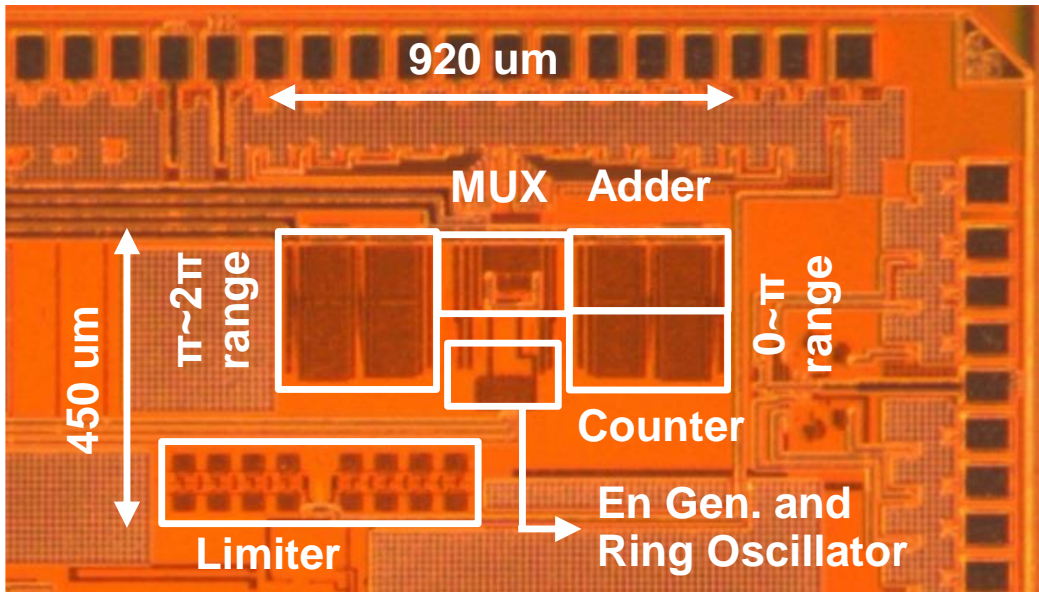
(a)
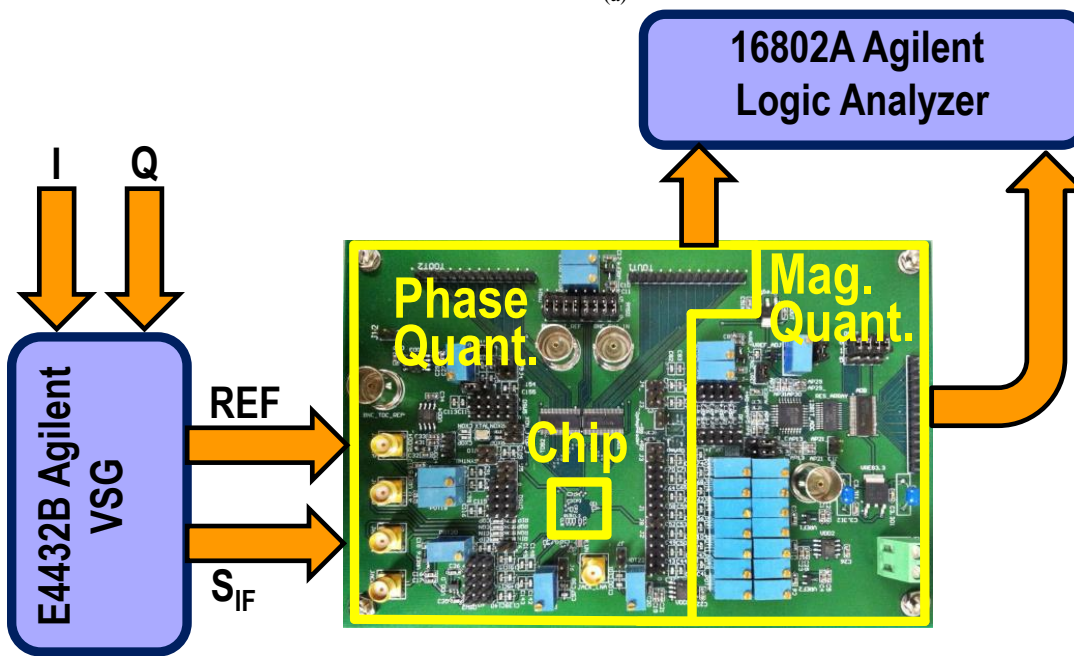
(b)

Figure 44 (a) Die photograph of phase quantizer, (b) Measurement setup

Conclusion

A study of polar receiver architectures and the CMOS implementation of a polar quantizer chip prototype were discussed. Comprehensive analytical studies followed by measurement results demonstrated up to 5.5dB of SQNR improvement compared to a traditional rectangular quantizer under Gaussian input distribution. In brief the advantages of polar receiver architecture is listed below:

- Higher SQNR under fading scenarios

- Saving one ADC

- Saving one mixer

- Using real mixer instead of quadrature mixer

- Using lower resolution ADC for amplitude quantization in comparison with I-Q quantization

- Power saving : phase quantizer consumes 1/3 power of a usual ADC

- Robustness against RF gain variation

- Relaxed RF gain control mechanism

- Amenable to technology scaling: Phase quantization resolution increases as the devices become faster

Also the challenges and system design considerations were discussed. In summary the challenges of polar receiver architecture are as follows:

- Phase quantization resolution depends on the counter upper limit and its clock frequency.

- Channel selection filtering should be partly done before phase and amplitude detection at intermediate (IF) frequency.

- To facilitate the design of on chip sharp channel selection filters, IF frequency should be chosen as low as possible.

- To enable digital filtering the quantizer should present a wide bandwidth to accommodate quantization of the interferers at offset frequencies.

- Due to nonlinear operation of phase and magnitude quantizer and bandwidth expansion of the resulting signals, the polar quantizer needs to accommodate wider bandwidth compared to I/Q quantizers, especially in the phase quantization path.

A prototype 10 bit polar quantizer was designed and fabricated in a 130nm CMOS. The phase quantizer was implemented using a dual path time-to-digital convertor (TDC). Within each path of TDC, 12 single edge TSPC counters count the zero crossing of a 6 phase high frequency clock signal. The 6 phases of the clock signal are generated using two quadrature-coupled three-stage ring oscillator to achieve 1 bit higher effective resolution. The quadrature operation of the ring oscillators are enforced by two quadrature cross coupled pair.

The resolution and INL/DNL curves as well as the transient response of the implemented phase quantizer are characterized and presented here. The TDC shows low power consumption, while its functionality is implemented such that this TDC is uniquely appropriate for true phase detection and quantization without phase ambiguity or significant dead-zone.

The system level measurements, showed superior SQNR of polar quantizer for complex Gaussian signals such as signals received in flat fading channels. The receiver also shows lower sensitivity to magnitude resolution and input attenuation.

References

[1] B. Carlson, "Communication Systems," McGraw-Hill Education, 2009.

[2] T. Sowlati, "Quad-band GSM/GPRS/EDGE polar loop transmitter," *IEEE J. Solid-State Circuits,* vol. 39, no. 12, pp. 2179-2189, 2004.

[3] M. R. Elliott, "A Polar Modulator Transmitter for GSM/EDGE," *EEE J. Solid-State Circuits,* vol. 39, no. 12, pp. 2190-2199, 2004.

[4] A. W. Hietala, "A quad-band 8PSK/GMSK polar transceiver," *IEEE J. Solid-State Circuits,* vol. 41, no. 5, pp. 1133-1141, 2006.

[5] M. Lee, "A 4-W Master–Slave Switching Amplitude Modulator for Class-E1 EDGE Polar Transmitters," *IEEE Trans. ,* vol. 55, no. 5, pp. 484-488, 2008.

[6] W. A. Pearlman, "Polar Quantization of a Complex Gaussian Random variable," *IEEE Trans. Commun.,* vol. 27, no. 6, pp. 892-899, 1979.

[7] P. W. Moo, "Uniform Polar Quantization Revisited," *ISIT Proc.,* p. 100, 1998.

[8] Z. H. Peric, "Asymptotic Analysis of Optimal Uniform Polar Quantization," *Int. J. Electronics and Communications,* no. 9, pp. 345-347, 2002.

[9] D. Antic, "Construction of Optimal Uniform Polar Switched Quantizer in Wide Volume Range," in *IEEE Workshop on Intelligent Data Acquisition and Advanced Computing Syst*, 2005.

[10] C. Chen, "A Low-Power 2.4-GHz CMOS GFSK Transceiver With a Digital Demodulator Using Time-to-Digital Conversion," *IEEE Trans. Circuits Syst. I: Regular Papers,* vol. 56, no. 12, pp. 2738-2748, 2009.

[11] B. Sklar, "Rayleigh Fading Channels in Mobile Digital Communication Systems Part I: Characterization," *IEEE Communications Magazine,* vol. 35, no. 7, pp. 90-100, 1997.

[12] T. S. Rappaport, Wireless Communications: Principles and Practice, New Jersey: Prentice Hall, 2001.

[13] I. L. Herlin, "Features extraction and analysis methods for sequences of ultrasound images," *Image and Vision ,* vol. 10, no. 10, pp. 673-682, 1992.

[14] M. Unser, "Automated detection of the tongue surface in sequences of ultrasound imagesM. Unser," *IEEE J. the Acoustical Society of America,* vol. 91, no. 5, pp. 3001-3007, 1992.

[15] "User equipment (UE) radio transmission and reception (Release 8)," 3GPP Tech. Spec. 36.101 v8.3.0., 2010.

[16] B. Razavi, RF Microelectronics, New Jersey: Prentice Hall, 1998.

[17] Q. Gu, RF System Design of Transceivers for Wireless Communications, New York: Springer, 2005.

[18] K. Martin, Digital Integrated Circuit Design, 1st Edition, New York: Oxford University Press, 1999.

[19] B. M. Helal, "A Highly Digital MDLL-Based Clock Multiplier That Leverages a Self-Scrambling Time-to-Digital Converter to Achieve Subpicosecond Jitter Performance," *IEEE J. Solid-State Circuits,* vol. 43, no. 4, pp. 855-863, 2008.

[20] M. Z. Straayer, "A 12-Bit, 10-MHz Bandwidth, Continuous-Time ΣΔ ADC with a 5-Bit, 950-MSs VCO-Based Quantizer," *IEEE J. Solid-State Circuits,* vol. 43, no. 4, pp. 805-814, 2008.

[21] M. Z. Straayer, "A Multi-Path Gated Ring Oscillator TDC with First-Order Noise Shaping," *IEEE J. Solid-State Circuits,* vol. 44, no. 4, pp. 1089-1098, 2009.

[22] M. Z. Straayer, *Noise Shaping Techniques for Analog and Time to Digital Converters Using Voltage Controlled Oscillators,* Massachusetts Inst. of Tech.: PhD thesis, 2008.

[23] J. Jansson, "A CMOS Time-to-Digital Converter with Better than 10ps Single-Shot Precision," *IEEE J. Solid-State ,* vol. 41, no. 6, pp. 1286-1296, 2006.

[24] R. B. Staszewski, "All-Digital TX Frequency Synthesizer and Discrete-Time Receiver for Bluetooth Radio in 130-nm CMOS," *IEEE J. Solid-State Circuits,* vol. 39, no. 12, pp. 2278-2291, 2004.

[25] D. K. Su, "An IC for Linearizing RF Power Amplifiers Using Envelop Elimination and Restoration," *IEEE J. Solid-State Circuits,* vol. 33, no. 12, pp. 2252-2258, 1998.

[26] J. Zhuang, "A Technique to Reduce Phase/Frequency Modulation Bandwidth in a Polar RF Transmitter," *Circuits and Systems I: Regular Papers, IEEE Transactions on ,* vol. 57, no. 8, pp. 2196-2207, 2010.

[27] Y.-H. Seo, "A 1.25 ps Resolution 8b Cyclic TDC in 0.13μm CMOS," *IEEE J. Solid-State Circuits,* vol. 47, no. 3, pp. 736-743, 2012.

[28] L. Vercesi, "Two-dimensions Vernier time-to-digital converter," *IEEE J. Solid-State Circuits,* vol. 45, no. 8, pp. 1504-1512, 2010.

[29] M. Lee, "A 9b, 1.25 ps resolution coarse-fine time-to- digital converter in 90 nm CMOS that amplifies a time residue,," *IEEE J. Solid-State Circuits,* vol. 43, no. 4, pp. 769-777, 2008.

[30] S. Henzler, "90 nm 4.7 ps-resolution 0.7-LSB single-shot precision and 19 pJ-per-shot local passive interpolation time-to-digital converter with on-chip characterization," in *IEEE ISSCC Dig. Tech. Papers*, San Francisco, 2008.

[31] R. B. Staszewski, "1.3 V 20 ps time-to-digital converter for frequency synthesis in 90-nm CMOS," *IEEE Trans. Circuits Syst. II, Express Briefs,* vol. 53, no. 3, pp. 220-224, 2006.

[32] K. Philips, "A Continuous-Time ΣΔ ADC with Increased Immunity to Interferers," *IEEE J. Solid-State Circuits,* vol. 39, no. 12, pp. 2170-2178, 2004.

[33] A. M. Bostamam, "Experimental Investigation of Undersampling for Adjacent Channel Interference Cancellation Scheme," *IEICE Trans. Commun.,* vol. 89, no. 9, pp. 2548-2554, 2006.

[34] T. Salo, "A 80-MHz Bandpass ΔΣ Modulator for a 100-MHz IF Receiver," *IEEE J. Solid-State Circuits,* vol. 37, no. 7, pp. 798-808, 2002.